Cellular Cycling, Carbon Utilization, and Photosynthetic Oxygen Production During Bicarbonate-Induced Triacylglycerol Accumulation in a Scenedesmus Sp.

Authors: Robert D. Gardner, Egan J. Lohman, Keith E. Cooksey, Robin Gerlach, & Brent Peyton

Gardner, Robert, Egan Lohman, Keith Cooksey, Robin Gerlach, and Brent Peyton. “Cellular Cycling, Carbon Utilization, and Photosynthetic Oxygen Production During Bicarbonate-Induced Triacylglycerol Accumulation in a Scenedesmus Sp.” Energies 6, no. 11 (November 2013): 6060–6076. doi:10.3390/en6116060.

AGU PUBLICATIONS

Water Resources Research

RESEARCH ARTICLE

10.1002/2014WR016503

Key Points:
- Revision of the model based on recent experiments
- Model recalibration using calcite and in situ concentration measurements
- Identification of areas for further research

Supporting Information:
- Supporting Information S1

Correspondence to:
J. Hommel,
johannes.hommel@iws.uni-stuttgart.de

Citation:
Hommel, J., E. Lauchnor, A. Phillips, R. Gerlach, A. B. Cunningham, R. Helmig, A. Ebigbo, and H. Class (2015), A revised model for microbially induced calcite precipitation: Improvements and new insights based on recent experiments, *Water Resour. Res.*, *51*, 3695–3715, doi:10.1002/2014WR016503.

Received 2 OCT 2014
Accepted 29 APR 2015
Accepted article online 5 MAY 2015
Published online 25 MAY 2015

A revised model for microbially induced calcite precipitation: Improvements and new insights based on recent experiments

Johannes Hommel[1], Ellen Lauchnor[2], Adrienne Phillips[2], Robin Gerlach[2], Alfred B. Cunningham[2], Rainer Helmig[1], Anozie Ebigbo[3], and Holger Class[1]

[1]Department of Hydromechanics and Modelling of Hydrosystems, University of Stuttgart, Stuttgart, Germany, [2]Center for Biofilm Engineering, Montana State University, Bozeman, Montana, USA, [3]Department of Earth Science and Engineering, Imperial College London, London, UK

Abstract The model for microbially induced calcite precipitation (MICP) published by Ebigbo et al. (2012) has been improved based on new insights obtained from experiments and model calibration. The challenge in constructing a predictive model for permeability reduction in the underground with MICP is the quantification of the complex interaction between flow, transport, biofilm growth, and reaction kinetics. New data from Lauchnor et al. (2015) on whole-cell ureolysis kinetics from batch experiments were incorporated into the model, which has allowed for a more precise quantification of the relevant parameters as well as a simplification of the reaction kinetics in the equations of the model. Further, the model has been calibrated objectively by inverse modeling using quasi-1D column experiments and a radial flow experiment. From the postprocessing of the inverse modeling, a comprehensive sensitivity analysis has been performed with focus on the model input parameters that were fitted in the course of the model calibration. It reveals that calcite precipitation and concentrations of NH_4^+ and Ca^{2+} are particularly sensitive to parameters associated with the ureolysis rate and the attachment behavior of biomass. Based on the determined sensitivities and the ranges of values for the estimated parameters in the inversion, it is possible to identify focal areas where further research can have a high impact toward improving the understanding and engineering of MICP.

1. Introduction

Microbially induced calcite precipitation (MICP) occurs when microbial metabolism alters the surrounding aqueous phase in a way that leads to precipitation of calcite. In this study, we focus on biofilm-based MICP via ureolysis by the bacterium *Sporosarcina pasteurii*.

MICP offers an engineering option that uses the controlled biofilm growth to achieve targeted calcite precipitation. In subsurface applications, this process is typically associated with a reduction of porosity and, even more importantly, of permeability. As an engineering technology, it can be used to alter hydraulic flow conditions and can be applied, for example, to cut off highly permeable pathways such as fractures, faults, or behind-casing defects in boreholes within a geological formation [*Phillips et al.*, 2013a; *Mitchell et al.*, 2013; *Phillips et al.*, 2013b].

S. pasteurii expresses the enzyme urease that catalyzes the hydrolysis reaction of urea ($(NH_2)_2CO$) into ammonia (NH_3) and carbon dioxide (CO_2). Aqueous solutions of ammonia become alkaline. Thus, the ureolysis reaction leads to an increase in pH. This shifts the carbonate balance in an aqueous solution toward higher concentrations of dissolved carbonate (CO_3^{2-}). Adding calcium (Ca^{2+}) to the system then results in the precipitation of calcium carbonate ($CaCO_3$). The overall MICP reaction is:

$$(NH_2)_2CO + 2H_2O + Ca^{2+} \rightarrow 2NH_4^+ + CaCO_3 \downarrow \quad (1)$$

In a porous medium, this process, which results in the aforementioned impacts on the hydraulic properties, depends on the interplay between biofilm growth, fluid dynamics, and reaction rates. Accordingly, a biofilm may develop which is characterized by an interaction of attachment, nutrient-dependent growth, decay, and detachment with the hydraulic conditions in the pore space. The density of a biofilm, i.e., the number of cells within a certain volume, is dependent on several factors such as shear stress or nutrient supply [*Paul et al.*, 2012]; data for these factors are not yet available for a reliable quantitative description.

A major difficulty for practical engineering applications of MICP is the predictive planning of its use and impact, since it involves a number of complex interacting processes. While the basic chemistry and the flow processes are known, it is the exact quantitative description of the interactions and, in particular, the influence of the biofilm and the developing precipitates that pose challenges to achieving predictability.

Models for simulating MICP processes have been developed by a number of authors [*Martinez et al*., 2014; *Barkouki et al*., 2011; *Cuthbert et al*., 2013; *van Wijngaarden et al*., 2011, 2013; *Ebigbo et al*., 2012], each of the models focusing on different processes. Often, the models developed are designed to match a series of experiments. Consequently, they focus on the processes of relevance in the corresponding experiments while neglecting other processes that might be relevant in the field.

The models presented by *Martinez et al*. [2014] and *Barkouki et al*. [2011] use a complex ureolysis rate equation [*Fidaleo and Lavecchia*, 2003] and a saturation-state dependent precipitation rate, while neglecting changes in permeability and the processes related to bacterial transport, growth, and decay. As a result, the ureolytic activity is assumed to be constant over time for each point in space and the distribution of urease in space is described by a Gamma distribution [*Martinez et al*., 2014] or an exponential function [*Barkouki et al*., 2011].

In *Cuthbert et al*. [2013], a first-order kinetic model is assumed for ureolysis, and bacterial transport and attachment are modeled. The precipitation rate is assumed to be stoichiometric to the ureolysis rate. The impact of MICP on the fracture transmissivity is measured in the experiment and included in the model depended on a reduction of the fracture aperture related to the volume of precipitated calcite.

Michaelis-Menten kinetics are used to model the ureolysis rate in *van Wijngaarden et al*. [2011, 2013] and, like *Cuthbert et al*. [2013], these authors assume that the precipitation rate is proportional to the ureolysis rate. The permeability is decreased based on the porosity reduction caused by the precipitated calcite. A Kozeny-Carman relationship is used to calculate the permeability. Bacteria are assumed to be homogeneously distributed in *van Wijngaarden et al*. [2011], while *van Wijngaarden et al*. [2013] account for attachment and detachment due to adsorption and desorption respectively. For special cases, *van Wijngaarden et al*. [2011, 2013] propose analytical solutions.

Ebigbo et al. [2012] developed a complex two-phase model including component transport, kinetic reactions, and reduction of porosity and permeability due to calcite precipitation and biofilm presence. This model uses a complex, biofilm-dependent ureolysis rate equation adapted from *Fidaleo and Lavecchia* [2003] and a calcite precipitation rate equation dependent on interfacial area and saturation state [*Zhong and Mucci*, 1989] as well as on dissolution kinetics [*Compton et al*., 1989; *Chou et al*., 1989]. Additionally, the model accounts for microbial processes such as attachment, substrate-dependent growth, decay, and detachment due to shear stress as well as for reduced porosity and permeability using a Kozeny-Carman relationship.

The model used in this study is an extension of the model presented in *Ebigbo et al*. [2012] after revisions such as the replacement of some of the fitted parameter values with updated literature values and an updated ureolysis rate equation [*Lauchnor et al*., 2015]. All rate equations, except the updated one for ureolysis, as well as the constitutive relationships used in *Ebigbo et al*. [2012] are assumed to be still valid.

The aims of this study are to investigate the predictive performance of the model developed in *Ebigbo et al*. [2012] for new column experiments and a 2-D radial flow experiment, to examine the effect of the implementation of a rate equation for ureolysis based on recent research on the ureolysis of *S. pasteurii* [*Lauchnor et al*., 2015], and to assess the range of fitting-parameter values obtained by inverse modeling. This should lead to the identification of areas to focus further research on, prioritizing future experimental investigations as well as defining strategies for the model development with the long-term perspective of a predictive field-scale MICP model. Figure 1 shows the sequential steps and objectives of this study.

2. Processes and Recent Experiments

2.1. Overview and Experiments

The original model was calibrated for columns using a certain set of conditions [*Ebigbo et al*., 2012]. However, after changes in the solution chemistry that were subsequently implemented in the experiments,

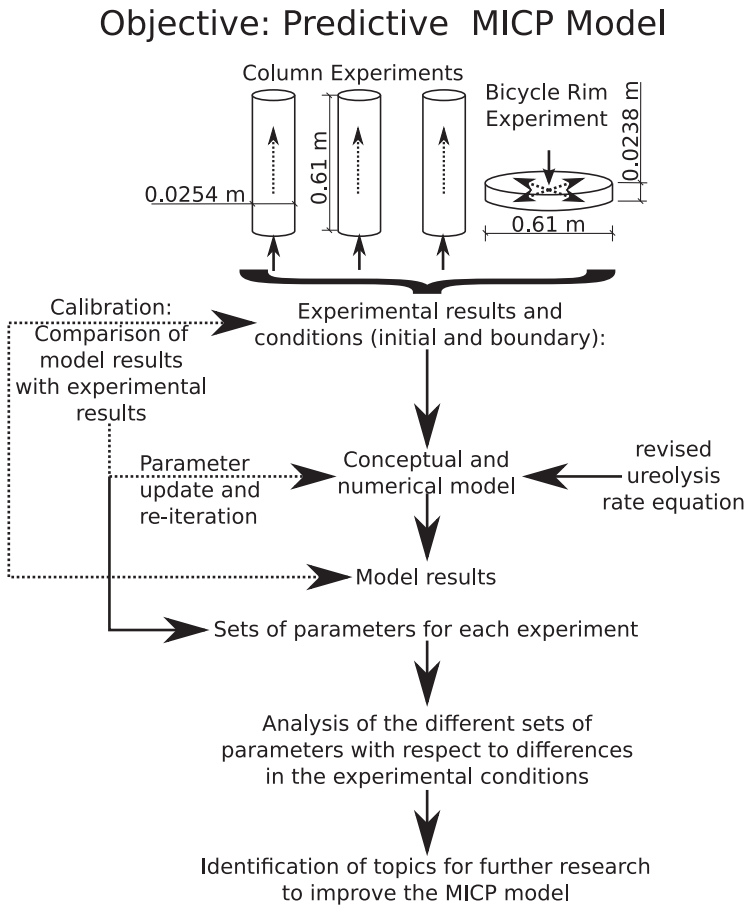

Figure 1. Overview of steps taken in this study.

modeling results no longer accurately predicted the measurements. For a substantial revision of the complex model of *Ebigbo et al*. [2012], the processes needed to be reconsidered in detail. Our considerations and hypotheses are based on a series of new experimental data from column experiments similar to those described in *Ebigbo et al*. [2012].

Data from three column experiments are used in the inverse modeling and determination of the fitting parameters. One column from the previous study, Column 4 (C4), is used to ensure reproducibility. Two more column studies were performed with modifications to the previous study. As these columns were operated as duplicates, they are denoted column D1 and column D2.

All columns were constructed from clear PVC pipe of 2.54 cm diameter and 61 cm length, filled with 40 mesh quartz sand (0.5 mm effective filtration size, manufacturer information, Unimin Corp., Emmet, ID), packed under water and vertically positioned. They were inoculated with *S. pasteurii* and subjected to a 16 h attachment period, after which a 24 h growth period was initiated by continuous addition of growth medium in an upflow configuration at 10 $\frac{\text{ml}}{\text{min}}$. Following the growth period, calcium additions commenced, consisting of injecting two pore volumes of calcium-containing medium, followed by a no-flow period to allow reaction and precipitation to occur. This mineralization period was followed by injection of growth medium to resuscitate the microorganisms and the procedure was repeated until calcium had been injected 22 times for column C4 and 30 times for columns D1 and D2.

Differences between the operating parameters for the columns C4, D1 and D2 are presented in supporting information Table S1, while the composition of injected fluids is given in supporting information Table S2. The first modification to the columns D1 and D2 was a reduction in the Ca^{2+} concentration to 0.33 M, which is equal to the molar concentration of urea in the mineralization medium. Second, the no-flow

period for biomineralization was reduced from 24 to 4 h as successfully implemented by [*Phillips et al*., 2013a] to increase Ca^{2+}-precipitation efficiency and decrease the time necessary to achieve the desired permeability reduction. Finally, the column studies used in the improved model calibration were constructed with five sampling ports at locations 10, 20, 30, 40 and 50 cm downstream of the inlet. Ports were made by drilling 1.252 cm holes in the PVC and securing rubber stoppers in the holes, allowing for sampling of pore fluid via a 23 gauge needle and 5 mL syringe. The sampling took place along the direction of flow and over time during the experiments, providing additional measurements for model calibration.

While columns D1 and D2 were operated, pore fluid was sampled from the ports at 1 h intervals during selected no-flow mineralization periods. The effluent pH, NH_4^+ and Ca^{2+} at the end of each mineralization and growth period were monitored, in addition to the NH_4^+ and Ca^{2+} measured in sampling ports over time during mineralization periods. Viable bacterial counts were performed on effluent samples, ensuring that *S. pasteurii* remained the active organism during the experiments. Finally, the columns were cut into eight sections to measure the precipitated calcite.

Additionally, a 2-D radial flow experiment was conducted in a radial flow reactor constructed from two plexiglass plates and a bicycle rim (BR), which enabled us to investigate the influence of a radial flow field on MICP. The radial flow experiment is valuable to investigate differences between different fluid-dynamic cases and make the model more broadly applicable to various environments, especially for field-relevant radial flow conditions.

The radial flow reactor was constructed from two 31 cm diameter, $\frac{1}{4}''$ Plexiglas plates that sandwiched a pack of the 40 mesh quartz sand, which was sealed on the outer diameter by squeezing the Plexiglas onto a metal ring (bicycle rim) with clamps. In between the Plexiglas and metal was a bead of Teflon putty which sealed the edge to prevent leaks when clamped tightly. Sixteen $\frac{1}{4}''$ NPT threads were inserted around the circumference of the top Plexiglas plate (outlet) as well as one thread in the center (inlet); these were all attached by barbed fittings to silicone tubing. The central inlet was connected via tubing to a peristaltic pump; the outlet tubes emptied into an elevated effluent collection tub.

The radial flow reactor was inoculated with 3 l of an overnight culture of *S. pasteurii* which was allowed to attach for 16.5 h and then subjected to a 12 h growth stage. After the growth period, calcium-containing medium was injected under constant flow conditions for 12 h followed by an overnight precipitation period. At the termination of the experiment, the Plexiglas plates were removed and the sand was sampled at 2.5, 4, 6.5 and 9 inches from the center in eight radial directions. Relevant experimental design parameters are summarized in supporting information Table S1, while supporting information Table S2 gives the composition of the injected fluids.

Microbially, whole-cell-catalyzed ureolysis is the driving force of MICP, increasing pH to the pKa of NH_3-NH_4^+ by the production of NH_3. At this pH, a substantial amount of carbonate is present in the solution (the pKa of HCO_3^--CO_3^{2-} is approximately one order of magnitude higher), which in turn, in the presence of calcium ions, can lead to a supersaturation of calcium carbonate in the solution, thereby promoting the precipitation of calcium carbonate. The dissociation coefficients of H_2CO_3 and NH_3 are calculated using relations given by *Millero et al*. [2007] and *Bell et al*. [2008] respectively.

Another key parameter is the distribution of biomass within the porous medium, since the presence of ureolytic microbes is a prerequisite for MICP. As the distribution of biomass is not exactly known for the MICP experiments, it is not possible to validate the equations governing the distribution of biomass directly by comparing with biofilm measurements. However, the ureolytic activity of the bacteria, which is monitored by measurement of the product NH_4^+ in recent column experiments, allows for an indirect evaluation of the model's ability to predict the biomass distribution.

2.2. Model Concept

The conceptual model for MICP follows the one presented by *Ebigbo et al*. [2012]. It accounts for two-phase multicomponent reactive transport on the continuum scale, including biofilm and calcite as solid phases. The considered reactions are pH-dependent dissociation reactions, microbial growth and decay as well as microbially catalyzed ureolysis and mass-transfer reactions between the different phases. Mass

Table 1. Component-Specific Reactive Source and Sink Terms as Implemented in the Conceptual Model[a]

Component	Source Term	Rates
Water	q^{w}	0
Total carbon	$q^{C_{tot}}$	$r_{diss} - r_{prec} + r_{urea}$
Sodium	q^{Na}	0
Chloride	q^{Cl}	0
Calcium	q^{Ca}	$r_{diss} - r_{prec}$
Urea	q^{u}	$-r_{urea}$
Total nitrogen	$q^{N_{tot}}$	$2r_{urea}$
Substrate	q^{s}	$-\frac{r_g^b + r_g^f}{M^s Y}$[b]
Oxygen	q^{O_2}	$-F\frac{r_g^b + r_g^f}{M^{O_2} Y}$[b]
Suspended biomass	q^{b}	$\frac{r_g^b - r_{dc}^b - r_a + r_d}{M^b}$
Biofilm	q^{f}	$\frac{r_g^f - r_{dc}^f + r_a - r_d}{M^f}$
Calcite	q^{c}	$r_{prec} - r_{diss}$
Precipitation rate of calcite	r_{prec}	$k_{prec} A_{sw} (\Omega - 1)^{n_{prec}}; \Omega \geq 1$[b]
Dissolution rate of calcite	r_{diss}	$(k_{diss,1} m_{H^+} + k_{diss,2}) A_{cw} (\Omega - 1)^{n_{diss}}; \Omega < 1$[b]
Interfacial area solid and water	A_{sw}	$A_{sw,0}\left(1 - \frac{\phi_c}{\phi_0}\right)^{\frac{2}{3}}$[b]
Interfacial area calcite and water	A_{cw}	$\min(A_{sw}, a_c \phi_c)$[b]
Saturation state of calcite	Ω	$\frac{m_{Ca^{2+}} \gamma_{Ca^{2+}} m_{CO_3^{2-}} \gamma_{CO_3^{2-}}}{K_{sp}}$[b]
Growth rate of biofilm	r_g^f	$\mu \phi_f \rho_f$
Growth rate of suspended biomass	r_g^b	$\mu C_w^b S_w \phi$
Specific growth rate	μ	$k_\mu Y \frac{C_w^s}{K_s + C_w^s} \frac{C_w^{O_2}}{K_{O_2} + C_w^{O_2}}$
Decay rate of biofilm	r_b^f	$\left(b_0 + \frac{r_{prec} M^{CaCO_3}}{\rho_c (\phi + \phi_f)}\right) \phi_f \rho_f$
Decay rate of suspended biomass	r_b^b	$b_0 \left(1 + \frac{K_{pH}}{m_{H^+}^2}\right) C_w^b S_w \phi$

[a]The ureolysis rate r_{urea} is discussed in detail in section 2.3 and shown in equation (4). Attachment and detachment rates r_a and r_d are discussed in section 2.4 and shown in equations (5) and (7) respectively. The other rate equations are summarized in the lower section of the table. Further details of those rates are discussed in *Ebigbo et al.* [2012].

[b]M^κ is the molar mass of κ, Y is the growth yield coefficient, F is the ratio of oxygen to substrate used for growth, k_{prec} and n_{prec} are empirical precipitation parameters [*Zhong and Mucci*, 1989], $k_{diss,1}$, $k_{diss,2}$, and n_{diss} are dissolution parameters [*Chou et al.*, 1989; *Compton et al.*, 1989], $A_{sw,0}$ is the initial interfacial area of solid and water phase, K_{sp} the calcite solubility product and γ_κ the activity coefficients of κ calculated using Pitzer equations [*Millero et al.*, 1984; *Wolf et al.*, 1989; *Clegg and Whitfield*, 1995] a_c the specific surface area of calcite, k_μ the maximum specific growth rate [*Connolly et al.*, 2013], b_0 the endogenous decay rate [*Taylor and Jaffé*, 1990], and K_{pH} is an empirical constant [*Kim et al.*, 2000].

transfer may occur between both fluid phases by mutual dissolution of water and CO_2 in the gas or the aqueous phase. It may also occur between the aqueous phase and the two 'solid' phases, biofilm and calcite denoted by subscripts (f) and (c) respectively, by attachment or detachment of biomass and precipitation or dissolution of calcite. The mobile components, denoted by superscripts κ, are water (w), dissolved inorganic carbon (C_{tot}), sodium (Na), chloride (Cl), calcium (Ca), urea (u), ammonium and ammonia (N_{tot}), substrate (s), oxygen (O_2), and suspended biomass (b). Substrate is the carbon and energy source of the bacteria and O_2 the electron acceptor. The consumption of both is linked to biomass growth by the yield coefficient Y; see Table 1. A pore-scale representation of the relevant processes and phases is shown in Figure 2.

The primary variables solved are the aqueous-phase pressure p_w, mole fractions x_w^κ of component κ in the water phase, and, for the solid phases biofilm and calcite, volume fractions ϕ_λ. All calcium carbonate is assumed to precipitate as calcite, since experimental investigations of *Phillips et al.* [2015]; *Mitchell et al.* [2013]; *Lauchnor et al.* [2013]; *Cuthbert et al.* [2012] confirmed by XRD measurements that calcite is the predominant polymorph of calcium carbonate precipitates forming under MICP conditions. In *Phillips et al.* [2013a], calcite and possibly vaterite were observed.

However, the CO_2-phase saturation is used as primary variable instead of the mole fraction of total inorganic carbon in water $x_w^{C_{tot}}$ whenever both fluid phases are present within the same control volume. All reactive and mass-transfer processes are incorporated in the component mass balance equations (2) and (3) by component-specific source and sink terms:

$$\sum_\alpha \left[\frac{\partial}{\partial t}\left(\phi \rho_\alpha x_\alpha^\kappa S_\alpha\right) + \nabla \cdot \left(\rho_\alpha x_\alpha^\kappa \mathbf{v}_\alpha\right) - \nabla \cdot \left(\rho_\alpha \mathbf{D}_{pm,\alpha} \nabla x_\alpha^\kappa\right)\right] = q^\kappa \tag{2}$$

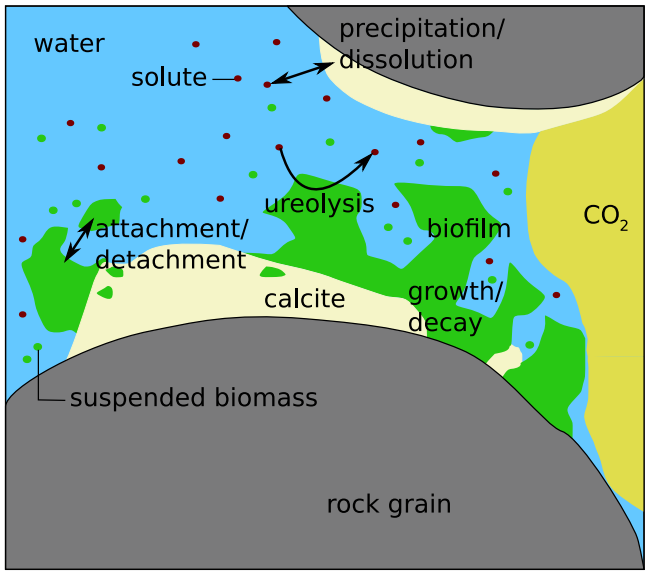

Figure 2. Schematic view of relevant processes and phases considered in the conceptual model.

here t is time, ϕ porosity, ρ_α, S_α, and $\mathbf{v}_\alpha$ the density, saturation and the velocity of phase α respectively, x_α^κ the mole fraction of component κ in phase α. $\mathbf{D}_{\mathrm{pm},\alpha}$ is the dispersion tensor of phase α in the porous medium, and q^κ is the source term of component κ due to biochemical reactions. The mass balances for the solid phases calcite and biofilm contain only a storage and source term since they are immobile:

$$\frac{\partial}{\partial t}(\phi_\lambda \rho_\lambda) = q^\lambda \tag{3}$$

here ϕ_λ and ρ_λ are volume fraction and density of the solid phase λ, and q^λ is the source term of phase λ due to biochemical reactions. The sources and sinks due to reactions q^κ and q^λ are specific to the components and given in Table 1.

The reaction rates $\left(\frac{\mathrm{mol}}{\mathrm{m^3 s}}\right)$ used to calculate the source terms are as follows:

1. r_{urea} is the rate of ureolysis (equation (4)),
2. r_{diss} and r_{prec} are the rates of calcite dissolution and precipitation,
3. $r_{\mathrm{g}}^{\mathrm{b}}$ and $r_{\mathrm{g}}^{\mathrm{f}}$ are the growth rates of suspended biomass and biofilm,
4. $r_{\mathrm{dc}}^{\mathrm{b}}$ and $r_{\mathrm{dc}}^{\mathrm{f}}$ are the decay rates of suspended biomass and biofilm,
5. and r_{a} (equation (5)) and r_{d} (equation (7)) are the attachment and detachment rates of biomass.

For more details on the reaction rates, we refer to *Ebigbo et al.* [2012] or the reaction-rate-equation summary in Table 1. However, since the rate of microbially catalyzed ureolysis and the rates of attachment and detachment are important in the context of this study, they will be discussed in sections 2.3 and 2.4.

2.3. Revised Ureolysis Kinetics

Most studies on ureolysis kinetics either focus on the kinetics of extracted enzyme [*Cuthbert et al.*, 2012; *Stocks-Fischer et al.*, 1999; *Tobler et al.*, 2011] or, when whole-cell systems are investigated, simplify kinetics to zero or first-order reaction rates depending only on urea concentrations [*Cuthbert et al.*, 2012; *Ferris et al.*, 2004; *Okwadha and Li*, 2010; *Tobler et al.*, 2011]. Few models for whole-cell systems use complex kinetics; e.g., *Ebigbo et al.* [2012] use a Michaelis-Menten-type ureolysis kinetic adapted from *Fidaleo and Lavecchia* [2003].

Urease extracted from *S. pasteurii* has been shown to have higher half-saturation coefficients than plant urease and an optimum rate at a pH of 8 [*Stocks-Fischer et al.*, 1999], whereas the optimal pH determined for the jack bean urease in *Fidaleo and Lavecchia* [2003] is at a pH of 7. In whole-cell systems, additional mass-transfer (transport) processes of reactants and products across the cell wall and regulatory processes within the cells are likely to influence the observed reaction rates in the bulk medium. This has been circumvented in continuum scale approaches through lumped apparent kinetic parameters.

The kinetic rates of biofilm cells might be different from the kinetics of suspended cells, as described in *Carrera et al.* [2004]. Even in the case of pure immobilized enzyme, there may be a decrease in the apparent reaction rates attributed to immobilization [*Bachmeier et al.*, 2002]. Other studies observed no significant difference between the kinetics of suspended and biofilm cells [*Shreve and Vogel*, 1993; *Mirpuri et al.*, 1997]. However, in thick biofilms, the diffusive transport of urea and NH_4^+ within the biofilm might significantly reduce the apparent ureolysis rate. In the light of the available information on this topic, we consider the

assumption of no significant difference between biofilm and suspended cell kinetics to be the most appropriate at this point, especially since no satisfactory parameterizations of the processes possibly leading to differences in the reaction kinetics are available on the Darcy scale.

In batch experiments, *Lauchnor et al*. [2015] investigated the influences of urea, NH_4^+, cell concentration, and pH of the medium on the ureolysis of whole cells of *S. pasteurii*. These new observations and measurements can be accounted for in the MICP model by adjusting the Michaelis-Menten kinetics and parameters:

$$r_{\text{urea}} = k_{\text{urease}}\, k_{\text{ub}}\, \rho_{\text{f}}\, \phi_{\text{f}}\, \frac{m^{\text{u}}}{m^{\text{u}} + K_{\text{u}}} \tag{4}$$

r_{urea} represents the revised rate of ureolysis according to *Lauchnor et al*. [2015], k_{urease} the revised maximum activity of urease adapted from *Lauchnor et al*. [2015], ρ_{f} and ϕ_{f} the density and volume fraction or biofilm respectively, k_{ub} the mass ratio of urease to biofilm as given in *Bachmeier et al*. [2002], m^{u} the molality of urea calculated from the water phase composition, and K_{u} is the half saturation constant for urea adapted from *Lauchnor et al*. [2015].

To convert the new half-saturation constant given by *Lauchnor et al*. [2015] $K = 355\ \frac{\text{mmol}}{\text{l}}$ to molalities $\frac{\text{mol}}{\text{kg}_{\text{H}_2\text{O}}}$, we assume that the concentrations used in the experiments did not affect the density. Thus, the half-saturation constant K_{u} in the model is set to $0.355\ \frac{\text{mol}}{\text{kg}_{\text{H}_2\text{O}}}$.

The value of the apparent urease activity k_{urease} in a whole-cell system is calculated by dividing the maximum reaction rate V_{max} by the urease content of a bacterial cell k_{ub}. According to *Bachmeier et al*. [2002], the urease content in *S. pasteurii* is at most 1% of the dry cell mass. As the cells in *Lauchnor et al*. [2015] are in late exponential phase with urea-replete conditions, it is assumed that they produce the maximum amount of urease possible. Thus, for further analysis, it is assumed that k_{ub} is equal to 0.01. To convert the units of V_{max} given in *Lauchnor et al*. [2015] from $\frac{\text{mmol}}{\text{CFU}\cdot\text{h}}$ (CFU standing for colony-forming units) to SI units for compatibility with the conceptual model, the same cell weight of $2.5\,10^{-16}\ \frac{\text{kg}}{\text{CFU}}$ is used as in *Ebigbo et al*. [2012], originally given in *Norland et al*. [1987]. The resulting updated value for k_{urease} is $706.7\ \frac{\text{mol}}{\text{kg}_{\text{biomass}}\cdot\text{s}}$, calculated from the value of the maximum reaction rate $V_{\text{max}} = 6.4\,10^{-9}\ \frac{\text{mmol}}{\text{CFU}\cdot\text{h}}$ given in *Lauchnor et al*. [2015].

As the observed ureolysis rates in *Lauchnor et al*. [2015] are directly proportional to the cell concentration, the exponent previously fitted in equation (11) [*Ebigbo et al*., 2012] is set to $n_{\text{ub}} = 1$ to achieve this linear dependence.

2.4. Biofilm-Hydraulics Interactions

Accumulation of biofilm in a porous medium reduces the pore space available for flow, thereby reducing the permeability. For constant flow, it increases the effective flow velocity in the pores and thus the pressure gradient required to maintain constant flow. This process continues until the pores are either completely filled with biofilm, blocking the flow, or a point is reached at which the increased detachment due to shear forces is in equilibrium with the accumulation of biomass by growth or attachment. Such an equilibrium will probably lead to local preferential flow paths where shear stress detaches the biofilm and neighboring regions are blocked by the biofilm. This can result in a subcontinuum-scale structure where different processes are dominant in each region on separate time scales. A dual-continuum approach as used in *Ebigbo et al*. [2010] is able to represent such subcontinuum-scale features on the Darcy scale. However, for the sake of computational efficiency and simplicity, as well as because of the lack of data available regarding biofilm transport processes, we refrain from using a dual-continuum approach in this study.

Microbial attachment is often modeled either as an adsorption equilibrium or according to colloid filtration theory. In the literature, there is a multitude of different approaches for describing attachment and detachment, depending on chemical conditions in the fluid or physical properties of the cells and the porous medium. For example, *Torkzaban et al*. [2008] observe that attachment of *Escherichia coli* increases with the ionic strength of the fluid. In microbially enhanced oil recovery simulations by *Nielsen et al*. [2014], microbial attachment is calculated either as adsorption following a Langmuir isotherm or according to the colloid filtration theory if the ratio of the cell size to the pore diameter is sufficiently large. However, in this study, it is assumed that the first-order-rate equation (see equations (5) and (6)) describing the transfer of biomass from the water phase (suspended biomass) to the biofilm phase by microbial attachment as given in *Ebigbo et al*. [2012] is still valid and only the values of the attachment coefficients have to be calibrated:

$$r_a = k_a C_w^b \phi S_w \tag{5}$$

$$k_a = c_{a,1}\phi_f + c_{a,2} \tag{6}$$

r_a stands for the rate of attachment, C_w^b for the mass concentration of suspended biomass in the water phase $\left(\frac{kg}{m^3}\right)$, S_w the saturation of the water phase, $c_{a,1}$ the attachment coefficient of suspended biomass to existing biofilm, and $c_{a,2}$ the general attachment coefficient of suspended biomass to any solid surface.

Detachment of biomass from biofilm is assumed to be proportional to the shear stress, approximated on the Darcy scale by using the absolute value of the water-phase potential gradient. Additionally, the growth rate contributes to the detachment rate, as vigorously growing biofilm is typically weaker and as such more susceptible to detachment. The detachment rate in this study is calculated as in *Ebigbo et al*. [2012]:

$$r_d = k_d \phi_f \rho_f \tag{7}$$

r_d is the rate of detachment and k_d the detachment coefficient:

$$k_d = c_{d,1}(\phi S_w |\nabla p_w - \rho_w \mathbf{g}|)^{0.58} + \frac{\phi_f}{\phi_0 - \phi_c}\mu \tag{8}$$

$c_{d,1}$ is a coefficient for the shear-stress-dependent detachment, $|\nabla p_w - \rho_w \mathbf{g}|$ the absolute value of the water-phase potential gradient, ϕ_0 the initial porosity, ϕ_c the volume fraction of calcite, and μ the specific growth rate of biomass, calculated based on double Monod kinetics dependent on both substrate and oxygen, see Table 1.

Since the detachment rate r_d is dependent on the potential gradient, it increases as the intrinsic permeability K is reduced during MICP by bio-clogging and precipitated calcite. It decreases in the following manner:

$$\frac{K}{K_0} = \left(\frac{\phi - \phi_{crit}}{\phi_0 - \phi_{crit}}\right)^3 \tag{9}$$

Here K_0 is the initial permeability, ϕ_{crit} the critical porosity at which the permeability is zero as estimated by *Ebigbo et al*. [2012], and ϕ_0 is the initial porosity. The porosity ϕ decreases as the volume fractions of biofilm and calcite increase:

$$\phi = \phi_0 - \phi_c - \phi_f \tag{10}$$

The total amount of biofilm in the system $\phi_f \rho_f$ is determined by biofilm volume fraction and density. ϕ_f is limited by the volume fraction available for biofilm $(\phi_0 - \phi_c)$ The smaller ρ_f,the smaller the maximum amount of attached biomass that can accumulate in the system. Additionally, ϕ_f of a given amount of biofilm is higher for low ρ_f, thereby increasing its influence on porosity and permeability. Reduced permeability leads to increased detachment, as $|\nabla p_w - \rho_w \mathbf{g}|$ increases. For complex 2-D or 3-D systems, low ρ_f might not necessarily increase detachment, as it inevitably would for 1-D systems, but lead to increased clogging and the formation of flow channels, increasing heterogeneity and dispersivity. Thus, the biofilm density is a key parameter of the model which greatly influences the amount of interaction between biofilm and flow processes.

The biofilm densities provided in the available literature vary over two orders of magnitude. *Melo* [2005] gives dry matter biofilm densities from 2.5 to 91 $\frac{kg}{m^3}$, *Zhang and Bishop* [1994] provide densities from 29 to 38 $\frac{kg}{m^3}$, while *Paul et al*. [2012] measure dry densities ranging from 5 to 39 $\frac{kg}{m^3}$. In *Taylor and Jaffé* [1990], the lowest value given is 2.5 $\frac{kg}{m^3}$, while the value used in the previous model is 10 $\frac{kg}{m^3}$ [*Ebigbo et al*., 2012]. As described in *Paul et al*. [2012], biofilm density is variable in space and time, changing with shear stress and growth conditions. However, to our knowledge, no parameterization is currently available that can duly account for these processes in the context of such a model. Thus, in the model, the biofilm density is a constant value representing both the dry cell density as well as the total dry biofilm density, neglecting the contribution of extracellular polymers.

2.5. Fitting Procedure

The number of fitting parameters is reduced compared with *Ebigbo et al*. [2012] by replacing some fitted values with literature values as discussed in section 4.1.

The fitting parameters of the conceptual model are the biofilm density ρ_f, the attachment coefficient of bacteria to existing biofilm $c_{a,1}$, and the attachment coefficient of bacteria to arbitrary solid surfaces $c_{a,2}$. It is

assumed that the first-order-rate equation (equation (5)) describing microbial attachment as given in *Ebigbo et al*. [2012] is still valid and only the values of the attachment coefficients have to be calibrated.

For some of the inverse model runs (section 3), k_{ub}, the parameter that has been identified in *Ebigbo et al*. [2012] as being most sensitive, is included in the set of calibration parameters to improve fitting. This can be additionally interpreted as a test of the hypothesis that the ureolysis rates of suspended and biofilm cells are equal, since the value of k_{urease} was calculated using this assumption (see section 2.3).

3. Model Calibration

Inverse modeling is used to recalibrate the numerical model implemented in the open-source simulator DuMu^x [*Flemisch et al*., 2011] using the experimental results of a variety of experimental setups. The grid used for the DuMu^x model is chosen in such a way that the grid nodes match the experimental sampling locations. Additionally, a grid-convergence study confirmed that the resolution of the grid used is sufficiently fine to avoid grid-induced artifacts as shown in supporting information Figure S1.

We perform inverse modeling rather than trial-and-error-based methods as used in *Ebigbo et al*. [2012] for the recalibration. Inverse modeling provides some analysis of parameter sensitivity and correlations between the different fitting parameters. To this end, iTOUGH2 and its PEST Protocol [*Finsterle*, 2007, 2011] were used as inverse model and coupled to the DuMu^x forward model using parameter input files. For details of the inverse modeling procedure, we refer interested readers to *Finsterle* [2007, 2011].

Various experimental results are used for the calibration of the model, including three column experiments, Column 4 (C4) [*Ebigbo et al*., 2012], two duplicate columns (D1, D2) and a 2-D radial flow experiment within a bicycle rim (BR). The latter is used to investigate possible influences of the flow field on the fitted parameter values, which would indicate inconsistencies in the conceptual model. For experiments C4 and BR, only the calcite volume-fraction distribution data at the end of the experiment were available for calibration; see supporting information Table S3. For experiments D1 and D2, additional in situ measurements of pore-fluid Ca^{2+} and NH_4^+ concentrations during the experiments at 10 cm intervals (i.e., 10, 20, 30, 40, and 50 cm from the injection point) are available and used as observation data for the inversions. These concentration measurements were conducted for each of the two experiments at six different points in time (i.e., 0, 0.5, 1, 2, 3 and 4 h after the end of selected Ca^{2+}-rich injections), each measurement being repeated six (for D1) or seven (for D2) times; see supporting information Tables S4–S7.

Finally, to be able to obtain parameter values averaged over all experimental setups, inverse modeling is performed using data of multiple experiments (C4, D2, BR), henceforth denoted (M). Since D2 is the experimental data set proving the most observations, the detailed discussions and plots (Figures 7–9 in section 4) focus on selected parameter sets obtained using this data set. These parameter sets are given in Table 2 while the respective parameter sensitivities as well as the correlations the "best fit" parameter set are shown in Table 3.

The initial guesses of the fitting parameters are based on parameter values given previously [*Ebigbo et al*., 2012] and for later inverse model runs based on estimates from previous inverse model runs. The other important parameters for inverse modeling, the standard deviations of the groups of observations, were estimated using experimentally determined standard deviations of the individual measurements. For the data sets D1 and D2 with in situ measurements of Ca^{2+}- and NH_4^+, the contribution of $CaCO_3$ to the objective function was weighted with a factor of 10 compared with those of the concentrations to compensate for the difference in the number of measurements (8 for $CaCO_3$, over 100 for Ca^{2+} and NH_4^+). This was done to achieve approximately equal initial sensitivity for each data set ($CaCO_3$, Ca^{2+}, and NH_4^+ measurements). Approximately equal sensitivity is considered necessary to ensure that every data set contributes to the parameter estimation, especially the application-relevant calcite data set which would otherwise be outnumbered. For inverse model runs where Ca^{2+} and NH_4^+ concentrations were considered a single data set, equal, averaged standard deviations were assumed as required by iTOUGH2, while for inverse model runs where each pulse was considered a separate data set, individual standard deviations for each pulse were used. The standard deviations were estimated based on a 5% reproducibility for the ion chromatography measurements.

The values obtained from the model calibration by inverse modeling for the biofilm density ρ_f range from 0.01 to 35 $\frac{kg}{m^3}$ (Figure 3), depending on the data set used for inverse modeling as well as the inverse

Table 2. Selected Parameter Sets Obtained by Inverse Modeling of Column Experiment D2 Data, Used for the Plots in Figures 7–9

Name	$c_{a,1}$ ($\frac{1}{s}$)	$c_{a,2}$ ($\frac{1}{s}$)	ρ_f ($\frac{kg}{m^3}$)	k_{ub}
low $c_{a,1}$ and $c_{a,2}$	$10^{-11.29}$	$10^{-14.59}$	4.80	0.0045
low ρ_f	$10^{-5.70}$	$10^{-6.66}$	0.062	0.01[a]
low k_{ub}	$10^{-4.81}$	$10^{-5.30}$	13.35	0.0014
best fit	$10^{-7.08}$	$10^{-6.07}$	6.9	0.00032

[a]k_{ub}=0.01 not fitted, but set according to *Bachmeier et al.* [2002].

modeling setup (i.e., the initial guess or the use of Ca^{2+} and NH_4^+ as one single observations set or the use of pulse-wise sets of observation). If the very low values obtained in the inverse model runs, which exclude k_{ub} from the set of fitting parameters, were neglected, the values for each experimental data set were within one order of magnitude. Calibration using the bicycle-rim data yielded exclusively higher ρ_f ranging from 6.4 to 35 $\frac{kg}{m^3}$ compared with the calibrations to any of the column experiments, where the highest value was 14.7 $\frac{kg}{m^3}$. The values of ρ_f obtained by using the multiexperiment data set M are 4.3 and 8.3 $\frac{kg}{m^3}$; note that M consists of all data from C4, D2 and BR, the calcite data of each experiment and the Ca^{2+} and NH_4^+ data of D2 receive initially approximately equal weight. ρ_f=4.3 $\frac{kg}{m^3}$ was obtained when the Ca^{2+} and NH_4^+ data of D2 were input as pulse-wise sets of observations, while ρ_f=8.3 $\frac{kg}{m^3}$ was obtained for the inverse model run on the data set M when considering the Ca^{2+} and NH_4^+ data of D2 a single observation set each. These values compare well with the lower values fitted against BR data and the intermediate range of the values fitted to the column experiments. They also match the parameter set "best fit," where the biofilm density obtained is 6.9 $\frac{kg}{m^3}$. Low biofilm densities are observed for calibration against any experiment when k_{ub} is excluded from the set of fitting parameters and set to the constant literature value of 0.01 [*Bachmeier et al.*, 2002].

Figure 4 shows the coefficient $c_{a,1}$ which varies between $10^{-12.81}$ and $10^{-1.81}$ $\frac{1}{s}$. However, most values for $c_{a,1}$ are in the much narrower range of $10^{-7.08}$ to $10^{-4.56}$.

The values of $c_{a,1}$ obtained by calibration against the combined data set of M, $10^{-5.78}$ (Ca^{2+} and NH_4^+ single observation sets each) and $10^{-4.56}$ $\frac{1}{s}$ (Ca^{2+} and NH_4^+ pulse-wise observation sets), are intermediate, while the "best fit" to D2, $c_{a,1}=10^{-7.08}$ $\frac{1}{s}$, is very low. Some calibrations using the column D2 data yield even lower values for $c_{a,1}$ ($10^{-12.81}$ and $10^{-11.92}$). For the bicycle-rim experiment, remarkably low values of $c_{a,1}=10^{-10}$ $\frac{1}{s}$ occur in sets of parameters in which the biofilm density is high (24 and 35 $\frac{kg}{m^3}$).

Figure 5 indicates that the parameter $c_{a,2}$ varies between $10^{-14.59}$ and $10^{-5.43}$ $\frac{1}{s}$. Note that the extremely low values of $10^{-14.59}$ and $10^{-14.27}$ $\frac{1}{s}$ obtained by fitting to column experiment D2 data are outliers. Most values are higher and range from $10^{-8.00}$ to $10^{-5.43}$ $\frac{1}{s}$. For almost all data sets, 10^{-6} $\frac{1}{s}$ is a representative value for the order of magnitude. In fact, for the bicycle-rim data set, the $c_{a,2}$ values are within one order of magnitude, between $10^{-6.39}$ and $10^{-5.43}$ $\frac{1}{s}$.

In most sets of parameters, $c_{a,2}$ is between 1 and 2.5 orders of magnitude lower than $c_{a,1}$. Contrary to this general trend, $c_{a,1}$ is several orders of magnitude lower than the corresponding $c_{a,2}$ in some of the fits using the bicycle-rim experiment data. This is also the case for the parameter set "best fit," where $c_{a,1}=10^{-7.08}$ $\frac{1}{s}$ is one order of magnitude lower than $c_{a,2}=10^{-6.07}$ $\frac{1}{s}$.

Table 3. Parameter and Data Sensitivities for the Parameter Sets Given in Table 2 and Direct Correlations for the Fitted Parameters of the "Best Fit" as Given by iTOUGH2

	ρ_f	$c_{a,1}$	$c_{a,2}$	k_{ub}	NH_4^+	Ca^{2+}	$CaCO_3$
Parameter and Data Sensitivity							
low $c_{a,1}$ and $c_{a,2}$	22328.0	615970.7	226.9	26.6	216384.9	368056.1	54111.2
low ρ_f	2293.4	263.4	549.0	[a]	1851.4	447.3	806.9
low k_{ub}	20.3	417.0	817.9	735.4	658.7	1294.6	37.3
best fit	59.2	583.1	642.2	1686.9	1086.9	1431.6	453.0

	ρ_f	$c_{a,1}$	$c_{a,2}$	k_{ub}
Direct Correlations for the "Best Fit"[b]				
ρ_f	1	−0.416	−0.804	0.277
$c_{a,1}$	−0.416	1	−0.504	0.473
$c_{a,2}$	−0.804	−0.504	1	0.502
k_{ub}	0.277	0.473	0.502	1

[a]k_{ub} not fitted, but set according to *Bachmeier et al.* [2002].
[b]The direct correlations for most other parameter sets are in the same range (± 0.2).

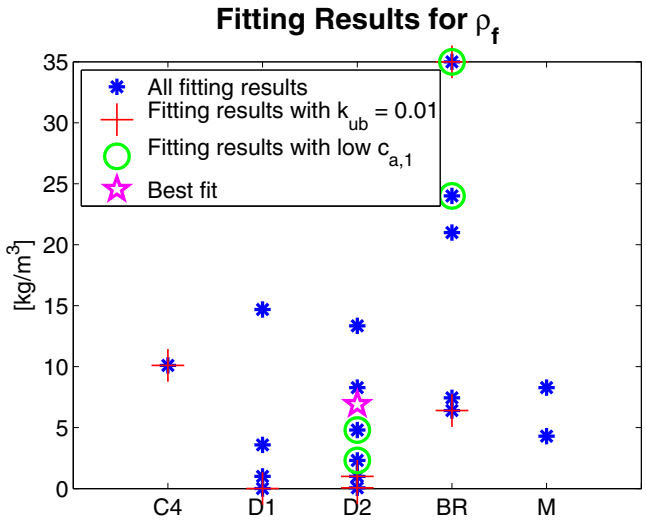

Figure 3. Values obtained for the biofilm density ρ_f for each experiment through parameter estimation using iTOUGH2. Multiple experiments (C4, D2, and BR) are combined in the data set M to fit averaged parameters values.

In the inverse model runs including k_{ub} as a fourth fitting parameter, the resulting values are all below the literature value of 0.01 given in *Bachmeier et al.* [2002] (see Figure 6). This result indicates that the apparent ureolysis rate or urease production of *S. pasteurii* growing as a biofilm is probably lower than the rate of suspended cells investigated in *Lauchnor et al.* [2015]. This might be caused by transport limitations as observed in *Bachmeier et al.* [2002] or due to a different metabolic activity of biofilm cells [*Carrera et al.*, 2004].

For the duplicate column experiments, the range of calibrated k_{ub} values was from 0.00032 to 0.0052, the "best fit" parameter value being the lowest. As in the case of for the biofilm density ρ_f, the values of k_{ub} obtained by fitting to bicycle-rim data are higher and range from 0.0026 to 0.0059. The values of k_{ub} obtained for the two inverse model runs using the data set M (0.001 and 0.0052) are in the range of the values fitted to D1 and D2. $k_{ub}=0.001$ was obtained when the Ca^{2+} and NH_4^+ data of D2 were input as pulse-wise sets of observations, while $k_{ub}=0.0052$ was obtained for the inverse model run on the data set M when considering these data a single observation set each.

If k_{ub} is included into the set of fitting parameters and the model is calibrated to the bicycle-rim data, the values of the biofilm density are moderate, while assuming a fixed $k_{ub}=0.01$ yields the lowest (6.4 $\frac{kg}{m^3}$) and the highest (35 $\frac{kg}{m^3}$) densities obtained for this experimental setup. If k_{ub} is included into the set of fitting parameters for the column experiments higher biofilm densities are obtained, while the values of the attachment coefficients do not change.

This can be explained by both k_{ub} and ρ_f occurring in the ureolysis rate equation, in which they are multiplied by each other, see equation (4). However, k_{ub} and ρ_f are not correlated ($r=0.277$ for the "best fit" parameter set, see Table 3), since the biofilm density also determines the volume fraction of a given mass of biofilm. Low densities lead to high volume fractions and a corresponding decrease in porosity and permeability. This increases the pressure gradient, thereby increasing detachment and limiting the maximum biomass ($\rho_f\phi_f$) present in the system.

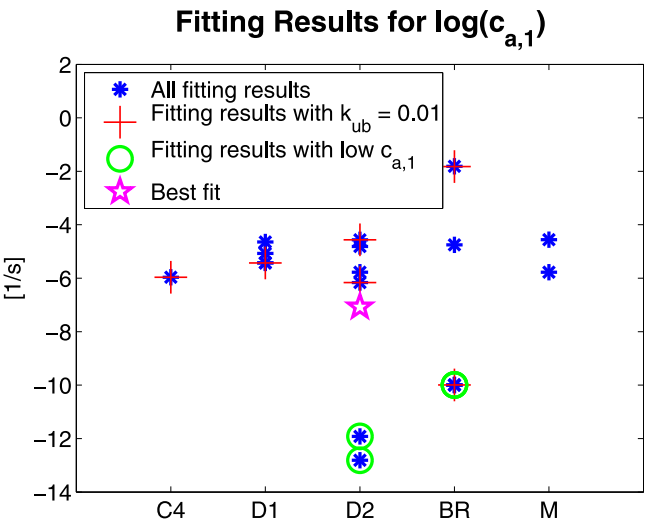

Figure 4. Values obtained for the attachment coefficient to biofilm $c_{a,1}$ through parameter estimation using iTOUGH2. Multiple experiments (C4, D2, and BR) are combined in the data set M to fit averaged parameters values.

S. pasteurii is aerobic and requires oxygen to synthesize urease [*Martin et al.*, 2012]. According to simulations, all oxygen is consumed during no-flow periods, which in reality would decrease the enzyme content of cells because de novo urease cannot be produced anaerobically. Hence, the low values for k_{ub} are comparable with the average urease contents of the

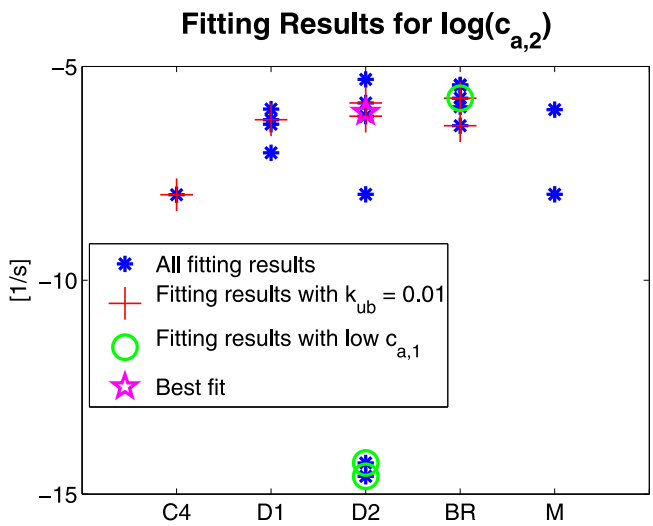

Figure 5. Values obtained for the attachment coefficient to arbitrary surfaces $c_{a,2}$ through parameter estimation using iTOUGH2. Multiple experiments (C4, D2, and BR) are combined in the data set M to fit averaged parameters values.

cells under alternatingly aerobic and anaerobic conditions, since the model assumes that the urease content of the cells is constant. The higher values of k_{ub} fitted using the BR data support this hypothesis as the constant flow injection scheme for this experiment reduces oxygen limitation of the cells. However, even in this experiment, the fitted values are considerably lower than the literature value of 0.01.

For a more detailed investigation of the parameters obtained, the simulation results for selected sets of parameters as given in Table 2 are plotted together with experimental data of column experiment D2 in Figures 7–9. The concentrations of Ca^{2+} and NH_4^+ shown in Figures 7 and 8 are measured and calculated at 0.3 m distance from the injection point. The data for the other measurement locations at 0.1, 0.2, 0.4, and 0.5 m distance are not shown here because of space constraints, but show similar trends.

Parameter sets with extremely low attachment coefficients $c_{a,1}$ and $c_{a,2}$ predict hardly any ureolysis and, hence, no calcite precipitation for the first three measured pulses. On the other hand, the parameter sets with higher $c_{a,1}$ and $c_{a,2}$ overestimate both ureolysis and precipitation and predict that nearly all Ca^{2+} would precipitate in all of the measurement pulses, while measurements show complete precipitation of dissolved calcium only for the last four pulses.

The "best fit" parameter set is able to predict most Ca^{2+} and NH_4^+ measurements. All other sets of parameters have in common that the reaction rates are overestimated although they were fitted to the same data set, which can best be seen in the comparison of measured and simulated NH_4^+ concentrations in Figure 8. Especially for later times, the simulated NH_4^+ concentrations right after the corresponding Ca^{2+}-rich injection are higher than the experimentally observed concentrations. This shows that the model predicts significant urea hydrolysis already during the injection phase while the experimental measurements do not confirm this prediction.

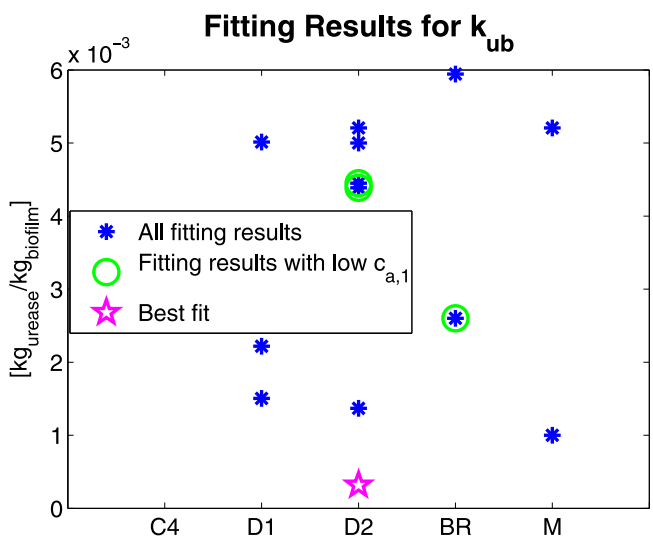

Figure 6. Values obtained for the urease content of biofilm k_{ub} through parameter estimation using iTOUGH2. Multiple experiments (C4, D2, and BR) are combined in the data set M to fit averaged parameters values. For C4, k_{ub} was not included in the set of fitting parameters for the inverse modeling.

With constant weight of the seven pulses of in situ measurements over time after a Ca^{2+}-rich injection, the first three pulses of measured Ca^{2+} and NH_4^+ concentrations do not match the data set D2 as seen in the plot for the parameter set "low attachment" in Figures 7 and 8. For the data set D1, a similar trend was observed (data not shown). Consequently, the weight of the first pulses was increased because attachment of

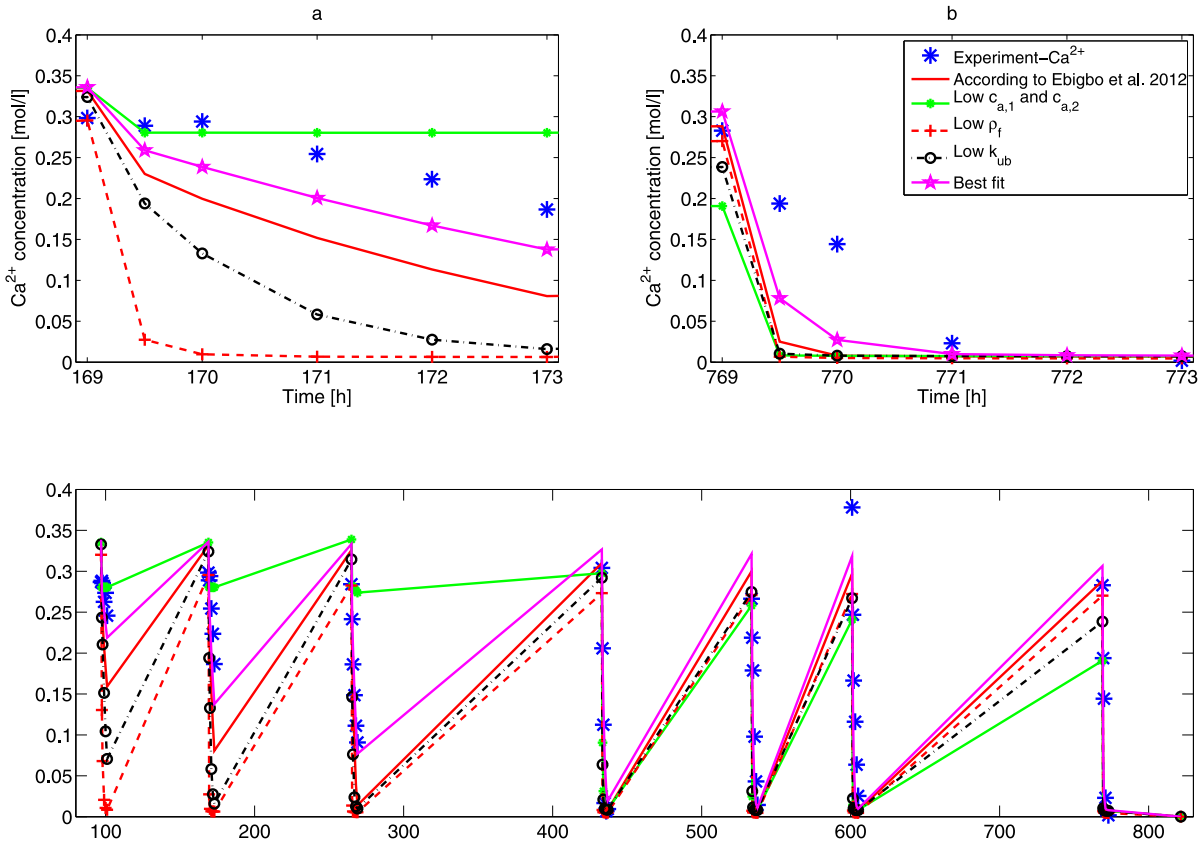

Figure 7. Simulation results for selected parameter sets in comparison to measured Ca^{2+} concentrations for column experiment D2 at 0.2 m distance from the injection point. (c) A total of seven measurement series were conducted after the end of Ca^{2+}-rich injection pulses. For a better temporal resolution shows (a) a zoom of the second measurement series and (b) one of the last (seventh). The parameter values corresponding to each set of parameters are given in Table 2.

bacteria is most relevant during the early times of the column experiment and thus determines the amount of attached biomass before significant growth occurs.

With higher weighting of the first three Ca^{2+}-rich injections, the fitted model is able to match the measured concentrations of NH_4^+ and Ca^{2+} more appropriately, although none of the parameter sets obtained resulted in model predictions matching the characteristic shape of both early and late measurements. For most measurements, however, the predictions for experiment D2 using the "best fit" parameter set (see Table 2) are closer to the measurements than for any other parameter set fitted using the data of experiment D2, see supporting information Table S8.

The final distribution of calcite obtained by modeling has a different shape compared with the experiments. Even when the weight of the calcite data set was very high, the estimated parameters did not significantly improve the shape of the modeled calcite distribution, especially in the inlet region. This is somewhat unexpected, because the sensitivity analysis provided by iTOUGH2 suggests that at least the inverse model runs leading to the parameter sets "low ρ_f" and "best fit" were sensitive to the $CaCO_3$ data, see Table 3. Most modeled volume fractions of calcite for D1 and D2 are higher than those measured, especially in the influent region. When the first 10 cm of the influent region are neglected, the two parameter sets, which were most sensitive to the $CaCO_3$ data, the "low ρ_f" and especially the "best fit" parameter set, result in modeled calcite distributions which are almost within the standard deviations of the experimental measurements. This result is additionally supported by the model predictions of both parameter sets resulting in very low residuals when compared with the calcite measurement (see supporting information Table S8). Figure 9 compares the measured and the simulated calcite distribution.

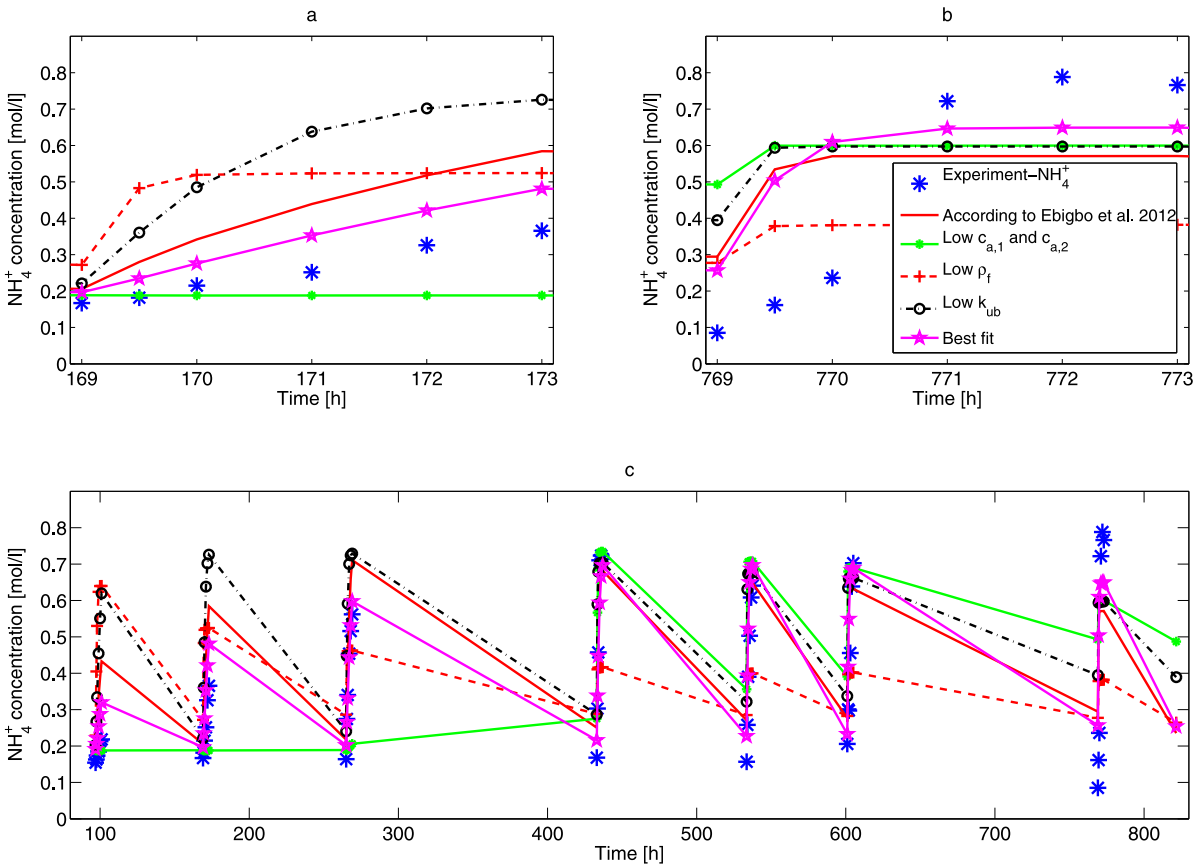

Figure 8. Simulation results for selected parameter sets in comparison to measured NH_4^+ concentrations for column experiment D2 at 0.2 m distance from the injection point. (c) A total of 7 measurement series were conducted after the end of Ca^{2+}-rich injection pulses. For a better temporal resolution shows (a) a zoom of the second measurement series and (b) one of the last (seventh). The parameter values corresponding to each set of parameters are given in Table 2.

As expected, the calibrated values of the fitting parameters are different depending on the experimental setup used for calibration, the initial guess of the parameters, and the weight (weighted standard deviation) of the observations. However, similar experimental setups, as in D1 and D2, lead to similar best-fit parameter values for identical inverse model parameters. The calibration results using multiple experimental data

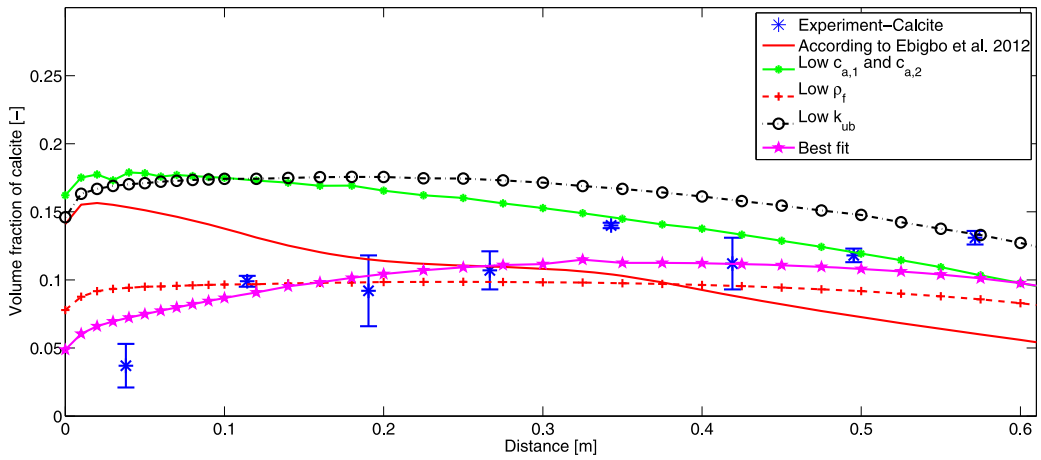

Figure 9. Simulation results for selected parameter sets in comparison to measured final volume fractions of calcite for column experiment D2. The error bars on the experimental values represent the standard deviation of triplicate measurements. The parameter values corresponding to each set of parameters are given in Table 2.

sets M yield intermediate parameter values. Thus, the values calibrated using the data set M can be interpreted as values averaged over the individual experimental setups. Consequently, these values represent a good approximation of the experiment-independent, true values of the fitting parameters. The values of the parameter set fitted to M that has the low value of $k_{ub}=0.001$ are additionally quite similar to the parameter set "best fit" of data set D2.

The calibrated parameter values (ρ_f and $c_{a,1}$) for the bicycle-rim data set encompass a wide range compared with the values calibrated to the other experimental data, except the extremely low attachment coefficients for some inverse model runs using D2 data. This might indicate that the inverse problem is ill-posed when using exclusively the limited BR data. For this experiment, no time-dependent measurements of pore fluids are available for calibration.

4. Discussion

Most fitted values of the biofilm density ρ_f compare well with the values given in the literature. Only some values fitted to D1 and D2 data are extremely low $\left(<1\,\frac{\mathrm{kg}}{\mathrm{m}^3}\right)$. However, these low values are obtained in inverse modeling runs which excluded the urease content of the cells k_{ub} from the set of parameters and assumed it to be equal to the maximum value given in *Bachmeier et al.* [2002]. In the inverse model runs including k_{ub} as fitting parameter, all estimates are lower than this maximum value. The calibrated values of the attachment coefficient $c_{a,2}$ are, in general, 2 orders of magnitude lower than the values given for *E. coli* in *Torkzaban et al.* [2008]. Both ρ_f and $c_{a,2}$ are species-dependent parameters, which limits the comparability of the calibrated values to literature data, because specific literature on the properties of *S. pasteurii* is sparse.

For most sets of parameters, except for the fits to the bicycle-rim experiment with k_{ub} set to the literature value of 0.01, the coefficient of attachment to existing biofilm $c_{a,1}$ is usually 1–2.5 orders of magnitude higher than the coefficient of attachment to arbitrary surfaces $c_{a,2}$. In the attachment coefficient equation (equation (6)), $c_{a,1}$ is multiplied by the volume fraction of biofilm, which is bounded by the value of the initial porosity. Thus, for realistic biofilm volume fractions (ϕ_f being typically less than 1% and initially no biofilm being present) and attachment-coefficient values as fitted, equation (6) is dominated by $c_{a,2}$ and the impact of $c_{a,1}\phi_f$ is negligible. The sets of parameters obtained from inverse modeling of the bicycle-rim experiment with k_{ub} set to 0.01 yield values for $c_{a,1}$ which are 4 orders of magnitude lower than the values for $c_{a,2}$, which would indicate that preferential attachment to biofilm does not occur during this experiment. Similarly, in the "best fit" parameter set, $c_{a,1}$ is one order of magnitude lower than $c_{a,2}$.Thus, preferential attachment to biofilm is not necessary to match the experimental results using the description of MICP currently implemented in the conceptual model.

The residuals between model predictions and the experimental results are reduced compared with the *Ebigbo et al.* [2012] model by some of the parameter sets, while other parameter sets lead to increased residuals (see supporting information Table S8). One explanation might be that the objective function has local minima which lead to nonoptimal parameter sets, depending on the initial guess of the fitted parameters. However, the parameter set "best fit" does not only have very low residuals when compared with the data set of experiment D2 used for calibration, but also matches quite well both the effluent pH measurements of experiment D2 (see supporting information Figure S5) which were not used as observation in inverse modeling as well as the calcite distributions of the other column experiments C4 and D1, see supporting information Figures S2 and S3.

Sections 4.2 and 4.3 discuss the experimental needs identified in this study as prerequisites for improving the conceptual understanding of MICP. Prior to this, the revised model is compared with the *Ebigbo et al.* [2012] model.

4.1. Comparison With the Previous Model

The main difference between the revised model used in this study and the MICP model developed previously [*Ebigbo et al.*, 2012] is the ureolysis rate equation. The previous model features complex Michaelis-Menten-type ureolysis kinetics adapted from *Fidaleo and Lavecchia* [2003]:

$$r_{\mathrm{urea,old}}=\frac{k_{\mathrm{urease,old}}}{1+\frac{m^{\mathrm{H}^+}}{K_{\mathrm{eu},1}}+\frac{K_{\mathrm{eu},2}}{m^{\mathrm{H}^+}}}\,k_{\mathrm{ub,old}}\left(\rho_f\,\phi_f\right)^{n_{\mathrm{ub}}}\,\frac{m^{\mathrm{u}}}{m^{\mathrm{u}}+K_{\mathrm{u,old}}}\,\frac{K_{\mathrm{NH}_4^+}}{m^{\mathrm{NH}_4^+}+K_{\mathrm{NH}_4^+}} \tag{11}$$

$r_{urea,old}$ is the rate of ureolysis as calculated in *Ebigbo et al*. [2012], $k_{urease,old}$ the maximum activity of urease from *Krajewska* [2009], m^{H^+} and $m^{NH_4^+}$ are the molalities of H^+ and NH_4^+, calculated from the water phase composition and the mole fractions respectively, $K_{eu,1}$ and $K_{eu,2}$ are speciation constants for the protonation and deprotonation of urease [*Fidaleo and Lavecchia*, 2003], $k_{ub,old}$ is the mass ratio of urease to biofilm and n_{ub} is an exponent accounting for nonlinear relations between biofilm and urease mass, both $k_{ub,old}$ and n_{ub} being fitting parameters in the model of *Ebigbo et al*. [2012], $K_{u,old}$ [*Krajewska*, 2009] is the half-saturation constant for urea as used in *Ebigbo et al*. [2012], and $K_{NH_4^+}$ is the product inhibition constant from [*Fidaleo and Lavecchia*, 2003].

This complex kinetic model accounts for a reduction of the maximum reaction rate by enzyme inactivation caused by nonoptimal pH and inhibition by high product (NH_4^+) concentrations as well as for varying biofilm mass and urea concentrations. Within the context of a MICP model, the main uncertainty of this ureolysis rate equation is that it was developed for the pure enzyme extracted from jack beans while, in most proposed MICP applications, whole cells of the bacterium *S. pasteurii* are used instead of pure enzymes.

The revised model uses the ureolysis rate equation (equation (4)) updated according to recent experimental investigations on the ureolysis kinetics of whole cells of *S. pasteurii* [*Lauchnor et al*., 2015]; see section 2.3. The new rate equation is specific for whole-cell systems of *S. pasteurii* and has neither pH dependency nor NH_4^+ inhibition since *Lauchnor et al*. [2015] demonstrated that neither process is influential to ureolysis in whole-cell systems of *S. pasteurii*.

Further, the maximum specific growth rate $k_\mu = 2.89\,10^{-5}\,\frac{1}{s}$, one of the parameters used to fit the model in *Ebigbo et al*. [2012], was replaced by a recently published literature value of $k_\mu = 4.1667\,10^{-5}\,\frac{1}{s}$ given in *Connolly et al*. [2013]. Additionally, the molecular diffusion coefficient in the water phase D_w was set to $1.587 \cdot 10^{-9}\,\frac{m^2}{s}$, as given in *Riquelme et al*. [2007]. Table 4 compares the parameters used in *Ebigbo et al*. [2012] with the parameters used in the revised model.

The performance of both the previous [*Ebigbo et al*., 2012] and the revised model proposed here in predicting the calcite distributions of various experiments (C4, D1 and BR) is shown in supporting information Figures S2–S4. Figures 7–9 give more detailed comparisons of the predictions of both models and column D2 data. These figures illustrate the improved match of model predictions and experimental observations gained with the revised model using the parameter set "best fit." This is confirmed by the calculated residuals given in supporting information Table S8.

The improvement of the revised model is a result of the increase in quantity and quality of the experimental data available, improving both the conceptual understanding of MICP as well as increasing the information for model recalibration. The ureolysis kinetics for the ureolysis of *S. pasteurii* [*Lauchnor et al*., 2015] resulted in the updated ureolysis rate equation which, together with the maximum specific growth rate for *S. pasteurii* [*Connolly et al*., 2013], allowed a reduction of the number of fitting parameters.

For the model recalibration, additional MICP experiments were available, providing measurements for an increased range of experimental conditions such as the injection strategy and injection rate (supporting information Table S1), the injected concentration (supporting information Table S2), and geometry (section 2.1 and Figure 1). Additionally, for the experiments D1 and D2, spatially and temporally resolved measurement of NH_4^+ and Ca^{2+} were available for recalibration, increasing the number of observations from the 8 calcite measurements up to more than 400 for each of the experiments.

Finally, the parameter estimation was more systematic as inverse modeling, rather than trial-and-error, methods were used for recalibration using the extended set of experimental observations as input, which resulted in additional insights, e.g., a sensitivity analysis of the model to both the observations used and the parameters estimated. The sensitivity analysis provided by iTOUGH2 indicated that the model is most sensitive to changes in the ureolysis rate equation. k_{ub} (and ρ_f instead, in case k_{ub} was excluded from the fitting parameters) was identified as the most sensitive parameter, followed by the attachment coefficients.

4.2. Ureolysis

All parameter sets including k_{ub} as a fitting parameter yield values smaller than the literature value of 0.01, indicating that the rate of ureolysis is overpredicted by equation (4) using the kinetic parameters for suspended cells from *Lauchnor et al*. [2015]. This is supported by the comparison of modeled with measured concentrations, as exemplarily shown in Figure 8, and by recalibrated sets of parameters with fixed $k_{ub} =$

0.01 resulting in low biofilm density, thereby favoring detachment and reducing the amount of ureolytic biomass in the simulations to match a lower reaction rate.

Another reason for the small k_{ub} estimates can be that *S. pasteurii* needs oxygen both to grow and produce urease [*Martin et al.*, 2012]. In the simulations of the column experiments, all oxygen is consumed during the batch periods following a Ca^{2+}-rich injection leading to anoxic conditions. These anoxic conditions could have led to less urease production in the biofilm, which would account for the lower average value of k_{ub} in the model. Additionally, the measurements show that the NH_4^+ concentration right at the end of the Ca^{2+}-rich injections is equal to the injected concentration of 0.177 $\frac{mol}{l}$, indicating that no significant amount of urea is hydrolyzed during flow, rather urea was hydrolyzed during no-flow periods. On the contrary, the model predicts that NH_4^+ concentrations already increase during the flow period for the later pulses for any set of parameters fitted (see Figures 8a and 8b).

This overestimation is caused by the model assumptions that the ureolysis rate is dependent on the bulk urea concentration (see equation (4)) and that the kinetic parameters are equal to those proposed by *Lauchnor et al.* [2015] (see section 2.3). Therefore, the use of suspended-cell kinetics will probably not be the final approach for MICP models, as most of the cells during MICP in subsurface systems are in biofilms [*Ebigbo et al.*, 2012; *Cuthbert et al.*, 2012]. It is important to investigate experimentally whether this overestimation is due to neglected additional mass transfer processes within the porous medium and the biofilm, as suggested by *Bachmeier et al.* [2002], or caused by a change in the kinetics resulting from the change in the growth mode, as suggested by *Carrera et al.* [2004]. Extracellular urease changes the apparent ureolysis kinetics of microbial cells in biofilms [*Klose and Tabatabai*, 1999] and the production of urease in cells within a biofilm might be different from that in suspended cells. Additionally, the assumption of well-mixed conditions is dependent on the heterogeneity of the porous medium. For the experiments, single-grain-size sand was used and packed carefully to avoid initial heterogeneities as described in section 2.1. Preferential flow paths and stagnant regions developing during the experiments could have lead to concentration and reaction-rate differences on the pore scale which are difficult to represent with an averaged bulk-concentration-dependent reaction rate in the Darcy-scale model.

A key step is to determine whether the reduced apparent reaction rates in biofilm systems occur due to mass-transfer limitations or due to significant differences in metabolism between biofilm and suspended cells. A combination of small to micro-scale experiments and pore-scale modeling is a promising approach for determining which of these processes is responsible for the observed discrepancies. If the discrepancies are caused by locally heterogeneous concentrations, the model can be improved by implementing additional equations describing the mass transfer between biofilm and liquid phase as well as diffusion within the biofilm. To give an example, mass transfer processes within the biofilm can be implemented using a double-continuum model as used in *Ebigbo et al.* [2010]. If locally heterogeneous concentrations are not able to explain the difference in the reaction rates observed, the biofilm-based kinetics parameters have to be determined experimentally for *S. pasteurii*. Alternatively, independently of what causes the discrepancy, upscaled biofilm-related kinetics parameters can be used which explicitly account for the metabolism of attached cells as well as heterogeneous concentrations and additional mass transfer. However, the conceptual understanding of biofilm-catalyzed ureolysis and of the potential influence of biofilm-fluid mass transfer needs to be improved. Further experimental research should focus especially on determining the apparent ureolysis rates of *S. pasteurii* biofilms and the resulting calcite precipitation rates, since these are the key processes of MICP.

4.3. Attachment and Biofilm Density

The best-fit attachment coefficients $c_{a,1}$ and $c_{a,2}$ vary over several orders of magnitude, indicating that the model is not very sensitive to them although the sensitivity analysis carried out by iTOUGH2 shows that the attachment coefficients have medium to high sensitivity compared with the other parameters fitted; see Table 3. Thus, a better knowledge of bacterial attachment would substantially improve the model. The model is especially sensitive to $c_{a,1}$ and $c_{a,2}$ at the beginning of the simulation, where the biofilm distribution is determined by attachment and not yet dominated by the interplay of growth and detachment, see Figures 7a and 8a. Especially for field-scale applications in which oxygen is not readily available, attachment of injected cells or cells detached from upstream regions might be the dominant process determining the distribution of biofilm. Experiments might show whether preferential attachment of *S. pasteurii* to existing biofilms, as assumed in equation (6), can be observed or not.

Table 4. Comparison of Revised, Refitted, and Other Parameter Values Used to the Values Given in *Ebigbo et al.* [2012]

Parameter	Unit	Revised Value	Revised Reference	*Ebigbo et al.* [2012]	*Ebigbo et al.* [2012]
ϕ_0		0.4	*Ebigbo et al.* [2012]	0.4	Measured
ϕ_{crit}		0	*Ebigbo et al.* [2012]	0	Estimated
K_0	m^2	$2 \cdot \times 10^{-10}$; $1.82 \cdot \times 10^{-10}$	Measured; *Ebigbo et al.* [2012]	$1.79-2.30 \cdot \times 10^{-10}$	Measured
ρ_c	$\frac{kg}{m^3}$	2710	*Ebigbo et al.* [2012]	2710	
ρ_f	$\frac{kg}{m^3}$	**0.01−35**	**Refitted**	10	Fitted
D_w	$\frac{m^2}{s}$	$\mathbf{1.587 \cdot \times 10^{-9}}$	*Riquelme et al.* [2007]	10^{-9}	
α_L	m	0.025	*Frippiat et al.* [2008]	0.025	*Frippiat et al.* [2008]
$A_{sw,0}$	$\frac{m^2}{m^3}$	5000	*Ebigbo et al.* [2012]	5000	Estimated
a_c	$\frac{m^2}{m^3}$	20000	*Ebigbo et al.* [2012]	20000	Estimated
k_{prec}	$\frac{mol}{m^2 s}$	$1.5 \cdot \times 10^{-10}$	*Zhong and Mucci* [1989]	$1.5 \cdot \times 10^{-10}$	*Zhong and Mucci* [1989]
n_{prec}		3.27	*Zhong and Mucci* [1989]	3.27	*Zhong and Mucci* [1989]
$k_{diss,1}$	$\frac{kg_{H_2O}}{m^3}$	$8.9 \cdot \times 10^{-1}$	*Chou et al.* [1989]	$8.9 \cdot \times 10^{-1}$	*Chou et al.* [1989]
$k_{diss,2}$	$\frac{mol}{m^2 s}$	$6.5 \cdot \times 10^{-7}$	*Chou et al.* [1989]	$6.5 \cdot \times 10^{-7}$	*Chou et al.* [1989]
n_{diss}		1	*Flukiger and Bernard* [2009]	1	*Flukiger and Bernard* [2009]
k_μ	$\frac{1}{s}$	$\mathbf{4.1667 \cdot \times 10^{-5}}$	*Connolly et al.* [2013]	$2.89 \cdot \times 10^{-5}$	Fitted
K_s	$\frac{kg}{m^3}$	$7.99 \cdot \times 10^{-4}$	*Taylor and Jaffé* [1990]	$7.99 \cdot \times 10^{-4}$	*Taylor and Jaffé* [1990]
K_{O_2}	$\frac{kg}{m^3}$	$2 \cdot \times 10^{-5}$	*Hao et al.* [1983]	$2 \cdot \times 10^{-5}$	*Hao et al.* [1983]
Y		0.5	*Seto and Alexander* [1985]	0.5	*Seto and Alexander* [1985]
F		0.5	*Mateles* [1971]	0.5	*Mateles* [1971]
b_0	$\frac{1}{s}$	$3.18 \cdot \times 10^{-7}$	*Taylor and Jaffé* [1990]	$3.18 \cdot \times 10^{-7}$	*Taylor and Jaffé* [1990]
K_{pH}	$(\frac{mol}{kg_{H_2O}})^2$	$6.15 \cdot \times 10^{-10}$	*Kim et al.* [2000]	$6.15 \cdot \times 10^{-10}$	*Kim et al.* [2000]
$c_{a,1}$	$\frac{1}{s}$	$\mathbf{1.55 \cdot \times 10^{-13} - 1.55 \cdot \times 10^{-2}}$	**Refitted**	0.0443	Fitted
$c_{a,2}$	$\frac{1}{s}$	$\mathbf{2.57 \cdot \times 10^{-15} - 3.72 \cdot \times 10^{-6}}$	**Refitted**	$9.19 \cdot \times 10^{-4}$	Fitted
$c_{d,1}$	$\frac{1}{s}$	$2.89 \cdot \times 10^{-8}$	*Ebigbo et al.* [2010]	$2.89 \cdot \times 10^{-8}$	*Ebigbo et al.* [2010]
k_{urease}	$\frac{mol}{kgs}$	**706.7**	*Lauchnor et al.* [2015]	41.7	*Krajewska* [2009]
K_u	$\frac{mol}{kg_{H_2O}}$	**0.355**	*Lauchnor et al.* [2015]	0.0173	*Krajewska* [2009]
$K_{eu,1}$	$\frac{mol}{kg_{H_2O}}$	Removed	*Lauchnor et al.* [2015]	$7.57 \cdot \times 10^{-7}$	*Fidaleo and Lavecchia* [2003]
$K_{eu,2}$	$\frac{mol}{kg_{H_2O}}$	Removed	*Lauchnor et al.* [2015]	$1.27 \cdot \times 10^{-8}$	*Fidaleo and Lavecchia* [2003]
$K_{NH_4^+}$	$\frac{mol}{kg_{H_2O}}$	Removed	*Lauchnor et al.* [2015]	0.0122	*Fidaleo and Lavecchia* [2003]
k_{ub}		**0.01**; **0.0014−0.0059**	*Bachmeier et al.* [2002]; **Refitted**	0.11	Fitted
n_{ub}		**1.0**	*Lauchnor et al.* [2015]	1.5	Fitted
T	°C	25	*Ebigbo et al.* [2012]	25	Constant

Further, the biofilm density is assumed to be constant in the conceptual model. In the literature, however, it is shown that the density of biofilms depends on various environmental factors such as exposure to shear stress, compaction of biofilm due to external stress, the history of exposure to external and shear stress during growth, and the type of electron acceptor available during growth [*Paul et al.*, 2012]. Biofilm density may also change with the thickness of the biofilm as shown in *Zhang and Bishop* [1994]. The validity of the assumption of a constant biofilm density used in the conceptual model has to be investigated in experiments, since the biofilm density strongly influences the amount of simulated attached biomass in the system. A better knowledge of the biofilm density is crucial to the success of any further investigation of the interactions of biofilm and hydraulic conditions. These interactions govern the distribution of catalytically active biofilm in the porous medium, thereby controlling the distribution of the precipitated calcite.

5. Final Remarks

Given the recent insight and experimental data on ureolysis and biofilm-hydraulics interactions, the model uncertainty is restricted by the currently insufficient knowledge of those processes and a lack of parameterizations which could crucially improve successful modeling of MICP. The focal points of future research as identified in this study are summarized in Table 5.

The difference between the experimental and modeled calcite distributions indicates that at least one relevant process for MICP is not yet implemented in sufficient detail in the conceptual model. Before a more detailed calibration of the numerical model is attempted, the conceptual understanding of all relevant processes, including the biofilm-catalyzed ureolysis, resulting calcite precipitation as well as the interplay of hydraulics and biofilm processes, has to be improved. Pore-scale investigations of ureolysis catalyzed by *S.*

Table 5. Focal Points to Improve the Conceptual Understanding of MICP by Targeted Experiments and Numerical Investigations as Identified in This Study

Focal Point	Suggested Investigation Method	Purpose of Research on This Focal Point
Biofilm-based ureolysis kinetics for *S. pasteurii*	experimental	Improve the understanding of biofilm-catalyzed ureolysis, determine the apparent ureolysis rate and find a suitable parameterization and the corresponding parameters
Density of *S. pasteurii* biofilms	experimental	Determine whether the assumption of constant biofilm density holds, if yes, give estimates of the density of *S. pasteurii* biofilms if not, identify the governing processes, and find a suitable parameterization and the corresponding parameters
Attachment of *S. pasteurii*	experimental	Determine whether preferential attachment to existing biofilm is relevant and estimate the attachment coefficient(s)
Accuracy of simplified models	numerical	Assess the modeling error of MICP models of different complexity in comparison to uncertainties resulting from unknown parameterizations of processes as well as unknown porosity and permeability for applications in the field

pasteurii biofilms might help determining which of the processes involved have to be considered in more detail.

Hence, a systematic experimental approach is needed for the investigation of the processes related to *S. pasteurii* biofilms in relevant conditions. Experiments are needed to derive apparent biofilm-based, volume-averaged parameter values which can be used for both engineering applications of MICP and numerical models used to design and evaluate future MICP experiments and applications.

Parallel to further experimentation, an investigation of simplified models designed to answer specific engineering questions is a promising approach for future modeling work, since knowledge of the relevant processes is limited and parameterizations are not available. For field-scale applications, the reduced accuracy of such simplified models is probably acceptable, since important site-specific modeling input parameters such as permeability and porosity are often not known in sufficient detail, resulting in an accuracy reduction which is greater than the reduction caused by simplifying model assumptions. Additionally, simplified models might prove to be computationally more efficient, thereby facilitating the use of MICP.

Acknowledgments
The numerical simulator DuMu^x used in this study can be obtained at http://www.dumux.org/download.php. The specific code used is available on request to the corresponding author. The International Research Training Group NUPUS is acknowledged for enabling this work within its framework. The authors further acknowledge the German Research Foundation DGF, the Netherlands Organization for Scientific Research NWO, and the Norwegian Research Council NRC for funding NUPUS. Funding for the experimental work was provided by the U.S. Department of Energy (DOE) grant DE-FE0004478, DE-FE0009599, and DE-FG02–13ER86571. Additionally, we thank Adam Rothman for help with the bicycle-rim and column experiments. Anozie Ebigbo acknowledges the UK Natural Environment Research Council, Radioactive Waste Management Limited and Environment Agency for the funding received for his project through the Radioactivity and the Environment (RATE) programme.

References

Bachmeier, K. L., A. E. Williams, J. R. Warmington, and S. S. Bang (2002), Urease activity in microbiologically-induced calcite precipitation, *J. Biotechnol.*, *93*(2), 171–181.

Barkouki, T. H., B. C. Martinez, B. M. Mortensen, T. S. Weathers, J. D. De Jong, T. R. Ginn, N. F. Spycher, R. W. Smith, and Y. Fujita (2011), Forward and inverse bio-geochemical modeling of microbially induced calcite precipitation in half-meter column experiments, *Transp. Porous Media*, *90*(1), 23–39, doi:10.1007/s11242-011-9804-z.

Bell, T. G., M. T. Johnson, T. D. Jickells, and P. S. Liss (2008), Ammonia/ammonium dissociation coefficient in seawater: A significant numerical correction, *Environ. Chem.*, *5*(3), 183–186, doi:10.1071/EN07032.

Carrera, J., I. Jubany, L. Carvallo, R. Chamy, and J. Lafuente (2004), Kinetic models for nitrification inhibition by ammonium and nitrite in a suspended and an immobilised biomass systems, *Process Biochem.*, *39*(9), 1159–1165, doi:10.1016/S0032–9592(03)00214-0.

Chou, L., R. M. Garrels, and R. Wollast (1989), Comparative study of the kinetics and mechanisms of dissolution of carbonate minerals, *Chem. Geol.*, *78*, 269–282.

Clegg, S. L., and M. Whitfield (1995), A chemical model of seawater including dissolved ammonia and the stoichiometric dissociation constant of ammonia in estuarine water and seawater from −2 to 40°C, *Geochim. Cosmochim. Acta*, *59*(12), 2403–2421.

Compton, R. G., K. L. Pritchard, and P. R. Unwin (1989), The dissolution of calcite in acid waters: Mass transport versus surface control, *Freshwater Biol.*, *22*(2), 285–288, doi:10.1111/j.1365–2427.1989.tb01101.x.

Connolly, J., M. Kaufman, A. Rothman, R. Gupta, G. Redden, M. Schuster, F. Colwell, and R. Gerlach (2013), Construction of two ureolytic model organisms for the study of microbially induced calcium carbonate precipitation, *J. Microbiol. Methods*, *94*(3), 290–299, doi:10.1016/j.mimet.2013.06.028.

Cuthbert, M. O., M. S. Riley, S. Handley-Sidhu, J. C. Renshaw, D. J. Tobler, V. R. Phoenix, and R. Mackay (2012), Controls on the rate of ureolysis and the morphology of carbonate precipitated by S. pasteurii biofilms and limits due to bacterial encapsulation, *Ecol. Eng.*, *41*, 32–40, doi:10.1016/j.ecoleng.2012.01.008.

Cuthbert, M. O., L. A. McMillan, S. Handley-Sidhu, M. S. Riley, D. J. Tobler, and V. R. Phoenix (2013), A field and modeling study of fractured rock permeability reduction using microbially induced calcite precipitation, *Environ. Sci. Technol.*, *47*(23), 13,637–13,643, doi:10.1021/es402601g.

Ebigbo, A., R. Helmig, A. B. Cunningham, H. Class, and R. Gerlach (2010), Modelling biofilm growth in the presence of carbon dioxide and water flow in the subsurface, *Adv. Water Resour.*, *33*(7), 762–781, doi:10.1016/j.advwatres.2010.04.004.

Ebigbo, A., A. J. Phillips, R. Gerlach, R. Helmig, A. B. Cunningham, H. Class, and L. H. Spangler (2012), Darcy-scale modeling of microbially induced carbonate mineral precipitation in sand columns, *Water Resour. Res.*, *48*, W07519, doi:10.1029/2011WR011714.

Ferris, F., V. Phoenix, Y. Fujita, and R. Smith (2004), Kinetics of calcite precipitation induced by ureolytic bacteria at 10 to 20°C in artificial groundwater, *Geochim. Cosmochim. Acta*, *68*(8), 1701–1710, doi:10.1016/S0016–7037(00)00503-9.

Fidaleo, M., and R. Lavecchia (2003), Kinetic study of enzymatic urea hydrolysis in the pH range 4–9, *Chem. Biochem. Eng. Q.*, *17*, 311–318.

Finsterle, S. (2007), iTOUGH2 user's guide, technical report no: LBNL-40040, Earth Sci. Div., Lawrence Berkeley Natl. Lab., Univ. of Calif., Berkeley, Calif.

Finsterle, S. (2011), iTOUGH2 universal optimization using the PEST protocol users guide, technical report no: LBNL-3698E, Earth Sci. Div., Lawrence Berkeley Natl. Lab., Univ. of Calif., Berkeley, Calif.

Flemisch, B., et al. (2011), DuMux: DUNE for multi-{phase, component, scale, physics,} flow and transport in porous media, *Adv. Water Resour.*, *34*(9), 1102–1112.

Flukiger, F., and D. Bernard (2009), A new numerical model for pore scale dissolution of calcite due to CO2 saturated water flow in 3D realistic geometry: Principles and first results, *Chem. Geol.*, *265*(1-2), 171–180, doi:10.1016/j.chemgeo.2009.05.004.

Frippiat, C. C., P. C. Pérez, and A. E. Holeyman (2008), Estimation of laboratory-scale dispersivities using an annulus-and-core device, *J. Hydrol.*, *362*(1-2), 57–68, doi:10.1016/j.jhydrol.2008.08.007.

Hao, O. J., M. G. Richard, D. Jenkins, and H. W. Blanch (1983), The half-saturation coefficient for dissolved oxygen: A dynamic method for its determination and its effect on dual species competition, *Biotechnol. Bioeng.*, *25*(2), 403–416, doi:10.1002/bit.260250209.

Kim, D. S., S. Thomas, and H. S. Fogler (2000), Effects of pH and trace minerals on long-term starvation of Leuconostoc mesenteroides, *Appl. Environ. Microbiol.*, *66*(3), 976–981.

Klose, S., and M. Tabatabai (1999), Urease activity of microbial biomass in soils, *Soil Biol. Biochem.*, *31*(2), 205–211, doi:10.1016/S0038–0717(98)00090-X.

Krajewska, B. (2009), Ureases I. Functional, catalytic and kinetic properties: A review, *J. Mol. Catalysis B Enzymatic*, *59*(1-3), 9–21, doi:10.1016/j.molcatb.2009.01.003.

Lauchnor, E. G., L. N. Schultz, S. Bugni, A. C. Mitchell, A. B. Cunningham and R. Gerlach (2013), Bacterially induced calcium carbonate precipitation and strontium coprecipitation in a porous media flow system, *Environ. Sci. Technol.*, *47*(3), 1557–1564, doi:10.1021/es304240y.

Lauchnor, E. G., D. Topp, A. E. Parker, and R. Gerlach (2015), Whole cell kinetics of ureolysis by Sporosarcina pasteurii, *J. Appl. Microbiol.*, doi:10.1111/jam.12804, in press.

Martin, D., K. Dodds, B. T. Ngwenya, I. B. Butler, and S. C. Elphick (2012), Inhibition of Sporosarcina pasteurii under anoxic conditions: Implications for subsurface carbonate precipitation and remediation via ureolysis, *Environ. Sci. Technol.*, *46*(15), 8351–8355, doi:10.1021/es3015875.

Martinez, B., J. De Jong, and T. Ginn (2014), Bio-geochemical reactive transport modeling of microbial induced calcite precipitation to predict the treatment of sand in one-dimensional flow, *Comput. Geotech.*, *58*, 1–13, doi:10.1016/j.compgeo.2014.01.013.

Mateles, R. I. (1971), Calculation of the oxygen required for cell production, *Biotechnol. Bioeng.*, *13*(4), 581–582, doi:10.1002/bit.260130411.

Melo, L. F. (2005), Biofilm physical structure, internal diffusivity and tortuosity, *Water Sci. Technol.*, *52*(7), 77–84.

Millero, F., F. Huang, T. Graham, and D. Pierrot (2007), The dissociation of carbonic acid in NaCl solutions as a function of concentration and temperature, *Geochim. Cosmochim. Acta*, *71*(1), 46–55, doi:10.1016/j.gca.2006.08.041.

Millero, F. J., P. J. Milne, and V. L. Thurmond (1984), The solubility of calcite, strontianite and witherite in NaCl solutions at 25°C, *Geochim. Cosmochim. Acta*, *48*, 1141–1143, doi:10.1016/0016–7037(84)90205-9.

Mirpuri, R., W. Jones, and J. D. Bryers (1997), Toluene degradation kinetics for planktonic and biofilm-grown cells of Pseudomonas putida 54G, *Biotechnol. Bioeng.*, *53*(6), 535–546, doi:10.1002/(SICI)1097-0290(19970320)53:6¡535::AID-BIT1¿3.0.CO;2-N.

Mitchell, A. C., A. J. Phillips, L. N. Schultz, S. Parks, L. H. Spangler, A. B. Cunningham, and R. Gerlach (2013), Microbial CaCO3 mineral formation and stability in an experimentally simulated high pressure saline aquifer with supercritical CO2, *Int. J. Greenhouse Gas Control*, *15*, 86–96, doi:10.1016/j.ijggc.2013.02.001.

Nielsen, S. M., I. Nesterov, and A. A. Shapiro (2014), Simulations of microbial-enhanced oil recovery: Adsorption and filtration, *Transp. Porous Media*, *102*(2), 227–259, doi:10.1007/s11242-014-0273-z.

Norland, S., M. Heldal, and O. Tmyr (1987), On the relation between dry matter and volume of bacteria X-ray analysis, *Microbial Ecol.*, *13*, 95–101.

Okwadha, G. D. O., and J. Li (2010), Optimum conditions for microbial carbonate precipitation, *Chemosphere*, *81*(9), 1143–1148, doi:10.1016/j.chemosphere.2010.09.066.

Paul, E., J. C. Ochoa, Y. Pechaud, Y. Liu, and A. Liné (2012), Effect of shear stress and growth conditions on detachment and physical properties of biofilms, *Water Res.*, *46*(17), 5499–5508, doi:10.1016/j.watres.2012.07.029.

Phillips, A. J., E. Lauchnor, J. J. Eldring, R. Esposito, A. C. Mitchell, R. Gerlach, A. B. Cunningham, and L. H. Spangler (2013a), Potential CO2 leakage reduction through biofilm-induced calcium carbonate precipitation, *Environ. Sci. Technol.*, *47*(1), 142–149, doi:10.1021/es301294q.

Phillips, A. J., R. Gerlach, E. Lauchnor, A. C. Mitchell, A. B. Cunningham, and L. H. Spangler (2013b), Engineered applications of ureolytic biomineralization: A review, *Biofouling*, *29*(6), 715–733, doi:10.1080/08927014.2013.796550.

Phillips, A. J., J. J. Eldring, R. Hiebert, E. Lauchnor, A. C. Mitchell, A. B. Cunningham, L. H. Spangler, and R. Gerlach (2015), Design of a meso-scale high pressure vessel for the laboratory examination of biogeochemical subsurface processes, *J. Pet. Sci. Eng.*, *126*, 55–62.

Riquelme, R., I. Lira, C. Pérez-López, J. A. Rayas, and R. Rodríguez-Vera (2007), Interferometric measurement of a diffusion coefficient: Comparison of two methods and uncertainty analysis, *J. Phys. D Appl. Phys.*, *40*(9), 2769–2776, doi:10.1088/0022–3727/40/9/015.

Seto, M., and M. Alexander (1985), Effect of bacterial density and substrate concentration on yield coefficients, *Appl. Environ. Microbiol.*, *50*(5), 1132–1136.

Shreve, G. S., and T. M. Vogel (1993), Comparison of substrate utilization and growth kinetics between immobilized and suspended Pseudomonas cells, *Biotechnol. Bioeng.*, *41*(3), 370–379, doi:10.1002/bit.260410312.

Stocks-Fischer, S., J. K. Galinat, and S. S. Bang (1999), Microbiological precipitation of CaCO3, *Soil Biol. Biochem.*, *31*, 1563–1571, doi:10.1016/S0038–0717(99)00082-6.

Taylor, S. W., and P. R. Jaffé (1990), Substrate and biomass transport in a porous-medium, *Water Resour. Res.*, *26*(9), 2181–2194, doi:10.1029/WR026i009p02181.

Tobler, D. J., M. O. Cuthbert, R. B. Greswell, M. S. Riley, J. C. Renshaw, S. Handley-Sidhu, and V. R. Phoenix (2011), Comparison of rates of ureolysis between Sporosarcina pasteurii and an indigenous groundwater community under conditions required to precipitate large volumes of calcite, *Geochim. Cosmochim. Acta*, *75*(11), 3290–3301, doi:10.1016/j.gca.2011.03.023.

Torkzaban, S., S. S. Tazehkand, S. L. Walker, and S. A. Bradford (2008), Transport and fate of bacteria in porous media: Coupled effects of chemical conditions and pore space geometry, *Water Resour. Res.*, *44*, W04403, doi:10.1029/2007WR006541.

van Wijngaarden, W. K., F. J. Vermolen, G. A. M. Meurs, and C. Vuik (2011), Modelling Biogrout: A new ground improvement method based on microbial-induced carbonate precipitation, *Transp. Porous Media*, *87*(2), 397–420, doi:10.1007/s11242-010-9691-8.

van Wijngaarden, W. K., F. J. Vermolen, G. A. M. Meurs, and C. Vuik (2013), A mathematical model for Biogrout, *Comput. Geosci.*, *17*(3), 463–478, doi:10.1007/s10596-012-9316-0.

Wolf, M., O. Breitkopf, and R. Puk (1989), Solubility of calcite in different electrolytes at temperatures between 10 and 60°C and at CO2 partial pressures of about 1 kPa, *Geochem. J.*, *76*, 291–301.

Zhang, T. C., and P. L. Bishop (1994), Density, porosity, and pore structure of biofilms, *Water Res.*, *28*(11), 2267–2277, doi:10.1016/0043–1354(94)90042-6.

Zhong, S., and A. Mucci (1989), Calcite and aragonite precipitation from seawater solutions of various salinities: Precipitation rates and overgrowth compositions, *Chem. Geol.*, *78*, 283–299.